



Supplement of

The importance of size ranges in aerosol instrument intercomparisons: a case study for the Atmospheric Tomography Mission

Hongyu Guo et al.

Correspondence to: Jose L. Jimenez (jose.jimenez@colorado.edu)

The copyright of individual parts of the supplement might differ from the article licence.

Table of contents:

Section 1-20, the following with text-based discussions:

Sect. 1: The cutoff sizes of selected submicron measurements

Sect. 4: AMS inlet configuration and performance

Sect. 5: AMS composition-dependent *CE*

**Sect. 8: PALMS detected particles and the operational size coverages for the
PALMS-AMP derived aerosol compositions**

Sect. 10: SAGA MC inlet transmission

Sect. 11: SAGA filter inlet transmission

Table S1-S2

Figure S1-S36

1. The cutoff sizes of selected submicron measurements

For AMS, the cut sizes in d_{va} are native and the other two sizes (d_{ta} , d_p) are calculated with Eqs. 1-2 in the main text. For URG, MOUDI, and SAGA MC, the cut sizes in d_{ta} are native, since the size selection is normally conducted in the transition regime. Specifically, given the native cutoff size in d_{ta} , the cut sizes in d_p for MOUDI are calculated using Eq. 5.28 in Hinds (2012):

$d_{50} = \sqrt{\frac{9\eta D_j (Stk_{50})}{\rho_p U C_c}}$. For circular jets such as MOUDI, 50% collection efficiency corresponds to Stokes Number, Stk_{50} , of 0.24. η is air viscosity, D_j is the nozzle size (0.78 mm) (Marple et al., 2014), U is air velocity (a nominal volumetric flow of 30 L min⁻¹ gives 26.16 m s⁻¹ with 40 nozzles at the size of 0.78 mm). The equation is also used to estimate the d_{50} for SAGA MC by dividing the formulas between the two conditions, and the base case gives $d_{ta,sea,50}$ of 1 μm (van Donkelaar et al., 2008) (discussed below at Sect. 10). Note that this method is not limited to calculating d_{50} but also other sizes so that the inlet transmission profile can be estimated for different pressure, temperature, or aerosol density, given an initial profile under known conditions.

Table S1: The cutoff sizes of AMS, URG PM₁ cyclones, MOUDI 1 μm stage impactor, and SAGA MC at two dry aerosol densities: 1.7 g cm^{-3} of ATom-2 campaign average and 0.9 g cm^{-3} of typical oily particles (Kuwata et al., 2012; Herring et al., 2015). Here only the upper side is listed. Since the conversion of d_p or d_{va} to d_{ta} is pressure dependent, d_{ta} at sea level, 6 km, and 12 km are calculated for AMS, MOUDI, and SAGA MC. The P at 6 km and 12 km are based on the U.S. standard atmosphere, 467 mbar and 185 mbar, respectively (NOAA, NASA, U. S. Air Force, 1976).

Dry Aerosol density		1.7 [g cm^{-3}]				0.9 [g cm^{-3}]			
		$d_{p,50}$	$d_{ta,sea,50}$	$d_{ta,air,50}$ (6/12km)	$d_{va,50}$	$d_{p,50}$	$d_{ta,sea,50}$	$d_{ta,air,50}$ (6/12km)	$d_{va,50}$
AMS	ATom-1&-2	443	599	624/670	753	836	789	785/775	753
	ATom-3	455	615	639/687	773	859	811	807/797	859
	ATom-4	564	758	782/837	959	1065	1006	1002/991	959
URG	Standard cut ^a	757	1010		1287	1069	1010		962
	Sharp cut ^a	788	1050		1340	1111	1050		1000
MOUDI 1 μm stage impactor	Sea level / 293 K ^b	749	1000		1273	1058	1000		952
	6 km / 293 K ^b	663		912	1127	970		912	873
	12 km / 293 K ^b	454		686	772	741		686	667
	6 km / 250 K ^c	612		845	1040	900		845	810
	12 km / 217 K ^c	371		569	631	616		569	551
SAGA MC	Sea level / 293 K ^a	749	1000		1273	1058	1000		952
	6 km / 250 K ^d	576		798	979	849		798	764
	12 km / 217 K ^d	328		507	558	551		507	496

^a At sea level ($P = 1013$ mbar, $T = 293$ K).

^b 293 K, a typical cabin temperature.

^c T is based on the U.S. standard atmosphere if the MOUDI impactor operates at ambient conditions.

^d The SAGA MC inlet operates at ambient conditions.

2. Comparison of the observable particle size ranges between instruments or inlets

Table S2: Comparison of the observable particle size ranges (i.e., contributing chemical composition information) between instruments or inlets for the conditions in ATom, a summary of the ATom-1 and -2 dataset. For the “submicron” category in the table, e.g., the AMS to URG volume ratio is calculated via $V_{phys,AMS} / V_{phys,URG}$, the ratio between the fraction seen by each instrument of the AMP volume. For the “AMP full size range” category, e.g., the AMS vs. AMP volume ratio is calculated via $V_{phys,AMS} / V_{phys}$. Lastly, for the “Overlap of AMS and PALMS-AMP” category, e.g., the overlap between AMS and PALMS-AMP vs. AMS is calculated via $V_{phys,AMS\&PALMS-AMP} / V_{phys,AMS}$, where $V_{phys,AMS\&PALMS-AMP}$ represents the volume measured by both AMS and PALMS-AMP. Six ratios are listed due to the three PALMS-AMP products discussed here. The PALMS-AMP 3-min and 60-min are calculated at the reported AMP size resolution (20 bins/decade), while the combined 4 bins (Fig. S13) are based on Froyd et al. (2019). Both volume and number fractions indicate the aerosol population represented by each instrument or inlet but don’t necessarily mean that all of the aerosol population is collected and measured (i.e., depending on the detection technique). These volume fractions are meaningful for comparing the coverage of the size distribution for particle mass products across aerosol instruments.

Category	Instrument or inlet	Volume [%]			Number [%]		
		Mean	Median	SD	Mean	Median	SD
Submicron	AMS vs. URG	95.1%	95.1%	14.4%	41.2%	40.7%	24.1%
	AMS vs. MOUDI	85.2%	87.7%	10.2%	43.9%	44.4%	23.7%
	AMS vs. SAGA MC ^a	96.6%	94.7%	13.9%	41.1%	40.6%	24.0%
AMP full size range (2.7 nm to 4.8 $\mu\text{m } d_p$)	AMS vs. AMP	67.8%	74.3%	22.5%	40.9%	40.5%	23.7%
	MOUDI vs. AMP	78.4%	87.0%	23.1%	89.4%	93.2%	10.7%
	SAGA MC vs. AMP ^a	70.3%	77.1%	23.9%	99.7%	100.0%	0.8%
	SAGA filter vs. AMP	96.2%	99.9%	12.9%	98.4%	99.1%	1.9%
	PALMS-AMP (3-min) vs. AMP	56.3%	57.7%	23.1%	6.3%	2.1%	10.3%
	PALMS-AMP (60-min) vs. AMP	73.5%	79.6%	21.4%	10.0%	4.7%	13.5%
	PALMS-AMP (4 bins) vs. AMP	76.1%	82.9%	21.4%	11.0%	5.2%	14.6%

Overlap of AMS and PALMS- AMP	vs. AMS (PALMS-AMP 3-min)	57.4%	61.2%	24.5%	10.5%	5.7%	12.6%
	vs. AMS (PALMS-AMP 60-min)	70.0%	76.2%	22.5%	17.4%	12.2 %	16.1%
	vs. AMS (PALMS-AMP 4 bins)	72.8%	79.2%	21.8%	21.3%	15.5%	18.3%
	vs. PALMS-AMP (3-min)	65.3%	69.8%	21.6%	96.0%	97.1%	4.0%
	vs. PALMS-AMP (60-min)	64.8%	70.2%	23.9%	97.9%	98.7%	2.7%
	vs. PALMS-AMP (4 bins)	65.8%	71.5%	24.2%	98.4%	99.0%	2.1%

^a Diffusion loss not considered for SAGA MC but expected to be minimal due to the very high airflows and relatively large and short sample line.

3. DC-8 sampling duration at each altitude

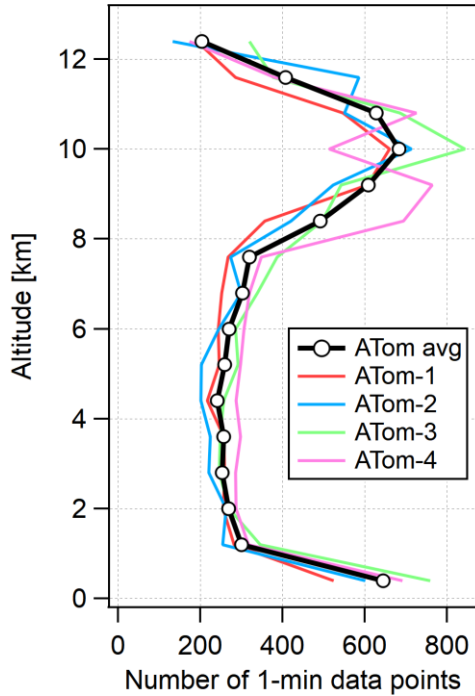


Fig. S1: Vertical 1-min data coverage during the ATom deployments. DC-8 sampled more often below 800 m and between 9 and 11 km compared to the intermediate altitudes. This sampling distribution is consistent with the generic ATom flight plan (longer sampling in the boundary layer and at the max altitude given air traffic control and fuel/weight considerations) and hence was also consistent throughout the ATom studies.

3. AMS total mass, OA/(OA+SO₄), ambient RH, and AMS inlet RH

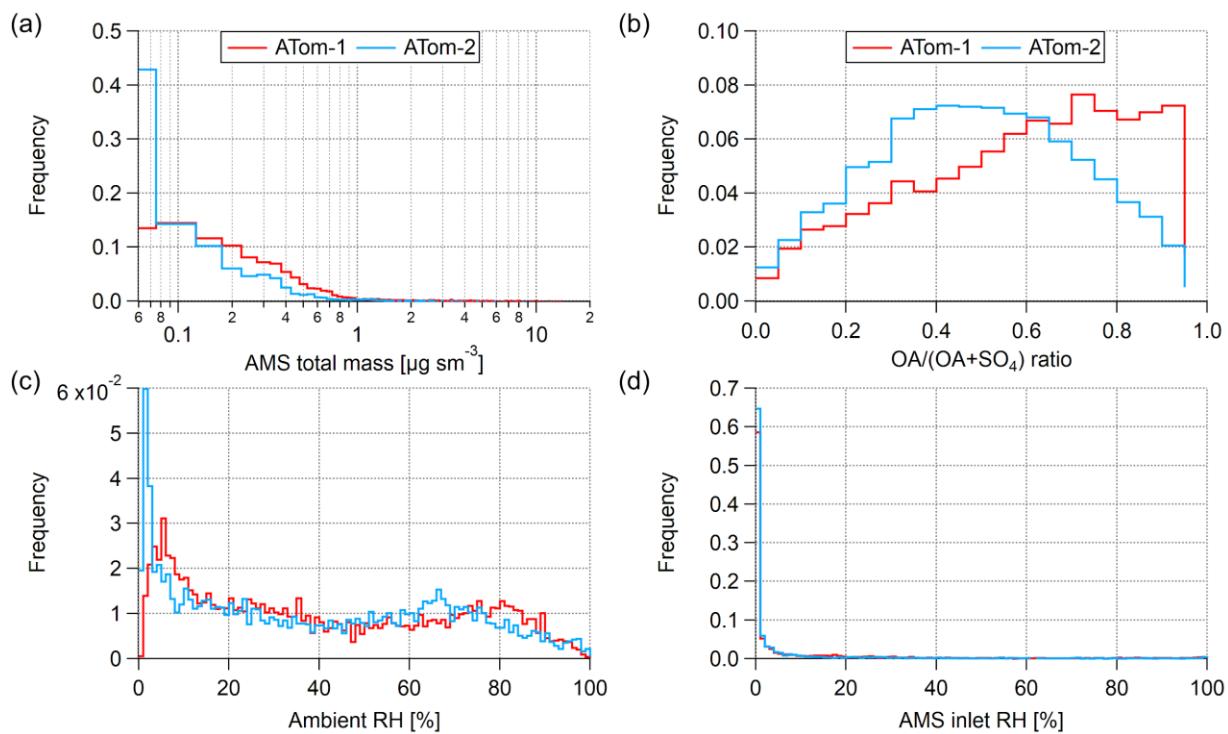


Fig. S2: The frequency distributions of (a) AMS detected total mass, (b) OA/(OA+SO₄) mass ratio, (c) ambient air RH, and (d) AMS inlet RH.

4. AMS inlet configuration and performance

Aerosols were sampled through a window-mounted NCAR High-Performance Instrumented Airborne Platform for Environmental Research (HIAPER) Modular Inlet (HIMIL) inlet (Stith et al., 2009), located 21.5 m behind the DC-8 nose. The inlet (tall HIMIL, 12”) (Rogers, 2011) was raised by 4” using a custom mounting plate, so that the sampling axis was 38.8 cm away from the plane skin, ensuring no contamination from the boundary layer of the plane at the sampling location, which has been previously characterized (Vay et al., 2003). The HIMIL is a sharp-edged diffuser inlet (which could potentially lead to directional losses for larger particles) (Baumgardner and Huebert, 1993), with an estimated slowdown of ambient air from the speed of the plane by a factor of 3-4 inside the diffuser (D. Rogers, NCAR, pers. comm.). The flow was then sampled into a straight, sharp-edged 3.8 mm internal diameter (ID) stainless steel tube pointing in the flow direction (called here the “secondary diffuser”, although no actual additional slowdown of the flow happens in this part of the inlet since a redesign in 2016). As described in the main text, the flow rate through this tube was prescribed to be 9 sL min⁻¹ (“s” stands for STP: $T = 273.15$ K, $P = 1013$ mbar), except at high altitude (> 9 km) where a smaller flow rate was chosen (15 vL min⁻¹; “v” stands for volumetric at in-situ T and P) to increase ram pressure and hence boost pressure just before the AMS inlet.

The inlet plumbing from the tip of the tube inside the HIMIL to the AMS is 1.5 m long (Fig. S3). To minimize residence time, the flow was operated turbulently (linear velocities between 5-15 m s⁻¹ and Reynolds numbers between 2000-5000) up to the takeoff of the excess flow. However, for the full range of diameters sampled by the AMS, the particle Reynolds number was always <1 and Dean numbers for bends were less <1000, hence calculated particle losses assuming mostly spherical particles are overall modest (Fig. S4). The overall transmission is mostly impacted by the 90° bend inside the HIMIL, the slight oversampling at the point where the main excess flow is taken out (“main takeoff,” Fig. S3), and the diffusion losses downstream of the last critical orifice. Overall, the calculated inlet plumbing transmission does not affect the higher end of the instrumental transmission curve used in this work (Fig. S4, bottom). It has a minor impact on the sub-100 nm size range of the transmission curve. However, since that part of the transmission curve a) does not really impact the volume analysis presented in this work (i.e., main text Sect 3.3) and b) was not determined in-situ for ATom (a 20% uncertainty at least; literature values are assumed (Zhang et al., 2004a; Knote et al., 2011)), adding this additional correction

does not seem warranted. Also, there are additional uncertainties regarding the turbulent loss calculations, shown in Fig. S4, that would probably require experimental confirmation.

The calculated transmission does not account for transmission prior to the first bend. However, as shown in Fig. S5, using a completely different inlet with the proven supermicron transmission (McNaughton et al., 2007) while maintaining the same conditions in the downstream plumbing, had no appreciable impact on the intercomparisons with other optical aerosol instruments during back-to-back inlet switches. So for the size range of interest, we assume that they are negligible.

As described in Bahreini et al. (2008), for reliable airborne AMS performance, especially over the large range of ambient pressure sampled with the NASA DC-8 (down to about 170 mbar), a device is needed that maintains constant pressure in front of the AMS aerodynamic lens and hence ensures a constant sampling flow and, more importantly, consistent aerodynamic focusing of the aerosol onto the AMS vaporizer (Zhang et al., 2004b; Huffman et al., 2005). Bahreini et al. (2008) accomplished this with a pressure controlled inlet (PCI) design consisting of a small volume between two critical orifices (C.O.; hereafter the first one encountered by the airflow is referred to as C.O. #1, and the bottom is referred to as C.O. #2) that is kept at constant pressure and placed in front of the AMS lens. Ideally, the pressure in the volume is lower at all times than ambient pressure, thus ensuring that both orifices remain under critical flow conditions. C.O. #2's size is then chosen to provide a suitable flow into the aerodynamic lens (ideally around $1.5 \text{ scm}^3 \text{ s}^{-1}$, cf. Section 2.2) while the top orifice has to be large enough to ensure enough excess flow at all altitudes.

The design in Bahreini et al. (2008) had two main drawbacks: a large residence time (~ 5 s) due to a large internal volume, which could impact the sampling of very volatile aerosol at altitude due to potential evaporation losses, and poor performance at the very low air pressures needed for operation on a plane such as the DC-8. The first one was addressed by reducing both the length and ID and using an improved internal takeoff design, to achieve an internal volume of only 3.5 cm^3 (vs. $\sim 30 \text{ cm}^3$ in the original design).

The reason for the poor performance at lower pressure is discussed in Chen et al. (2007): for a flat critical orifice, reducing inlet pressure leads to a larger angle for the air expanding behind the orifice and eventually to recirculation and particle loss due to impaction. This depends on the exact parameters of the expansion, so that in general smaller orifice sizes and smaller tubing sizes

downstream will increase the likelihood of losses. How this works in practice is illustrated in Fig. S6: for the regular, ground-based AMS with a PM₁ lens at 1 atm, the large particle losses are mostly at the back of the C.O. (Williams et al., 2013), due to the small orifice and small expansion tube. For the larger C.O. #1 facing ambient pressure used in both Bahreini et al. (2008) and this work, even at low pressures, losses at this orifice are less critical (Fig. S6). This is also the case for newer AMS lens designs (Williams et al., 2013; Peck et al., 2016) with optimized expansion geometries.

On the other hand, for C.O. #2, the one at the bottom of the PCI and facing the aerodynamic lens, as the pressure in the PCI decreases, an expansion into a small tube ($\frac{1}{4}$ " outer diameter (OD), as used by (Bahreini et al., 2008)) leads to significant losses at low pressures (Fig. S6). To address this, a double diffuser volume was designed and built in collaboration with X. Wang and P. McMurry (University of Minnesota) (Fig. S7, Volume A1), which allowed for a controlled expansion into a 30 mm diameter volume. This design was successfully flown on the ARCTAS (Jacob et al., 2010) and DC3 (Barth et al., 2015) missions with a PCI pressure of 130 mbar and minimal losses (Cubison et al., 2011; Yang et al., 2015). However, both the $\frac{1}{4}$ " OD tubing present in this design and possibly the overall gradual transition to larger diameters in the initial diffuser can lead to significant evaporation artifacts for the pure dry ammonium nitrate aerosol used to calibrate the AMS, as illustrated in Fig. S8. While there is no evidence that this issue impacted ambient, lower-volatility aerosol, it introduced a significant additional uncertainty on the AMS sensitivity calibration. Hence Volume A was first modified (Volume A2, which had a single fitting as an inlet/C.O. mount) and two other designs (B and C in Fig. S7) were tested in subsequent airborne missions (both on the NASA DC-8 and NCAR/NSF C-130). While Volume A2 still exhibits some evaporation artifacts the later designs did not (Fig. S8), and the transmission of Volume C matched the performance of the Volume A2, as shown in Fig. S9. Nevertheless, it should be noted that overall the performance of both Volume B and C is worse than the originally designed Volume A1, which worked well up to 300 μ m orifice size, for reasons that are still unclear.

Hence for ATom (starting with the Aug 12, 2016, flight on ATom-1, Volume A2 was flown previously to that), Volume C was flown using a 220 μ m C.O. for C.O. #2. As Fig. S9 and this manuscript overall make clear, this resulted in reproducible near-reference PM₁-aerodynamic lens performance (Hu et al., 2017) with no evaporation artifacts (Fig. S8), but with the drawback that

constant pressure (in the expansion volume) could only be maintained up to a pressure altitude of about 9 km. While not ideal, this configuration guaranteed that, even at max DC-8 altitude, the pressure in the aerodynamic lens would never go below 1.33 mbar, and hence the aerodynamic focusing into the vaporizer was not substantially impacted (but some additional diffusional losses are shown in Fig. S4).

It should be noted that overall, based on the calculations shown in Fig. S6 and the improved geometry interfacing the PCI with the aerosol lens, both lower PCI pressures and slightly above the reference performance (Hu et al., 2017) should be possible. The observed performance is likely related to the impact of mechanical imperfections on the overall flow profile through the PCI, something that is not unusual for aerodynamic focusing devices (Schreiner et al., 1999) and that is currently being further characterized. The improvement in transmission from ATom-1&2&3 to ATom-4 is likely related to this.

In summary, the current CU-AMS aircraft inlet provides to our knowledge the best transmission of a PM_{10} lens-based airborne system with reproducible performance up to 13 km and very low residence times over the full atmospheric column. Recently, Molleker et al. (2020) have described a new airborne AMS inlet system based on $PM_{2.5}$ lens with a larger size range and comparable residence times to the system described here, although it is currently unclear how well it works for small particles and how well it performs in the field. But it highlights that there are realistic options to expand the airborne size range in the future beyond the limits currently described in this work.

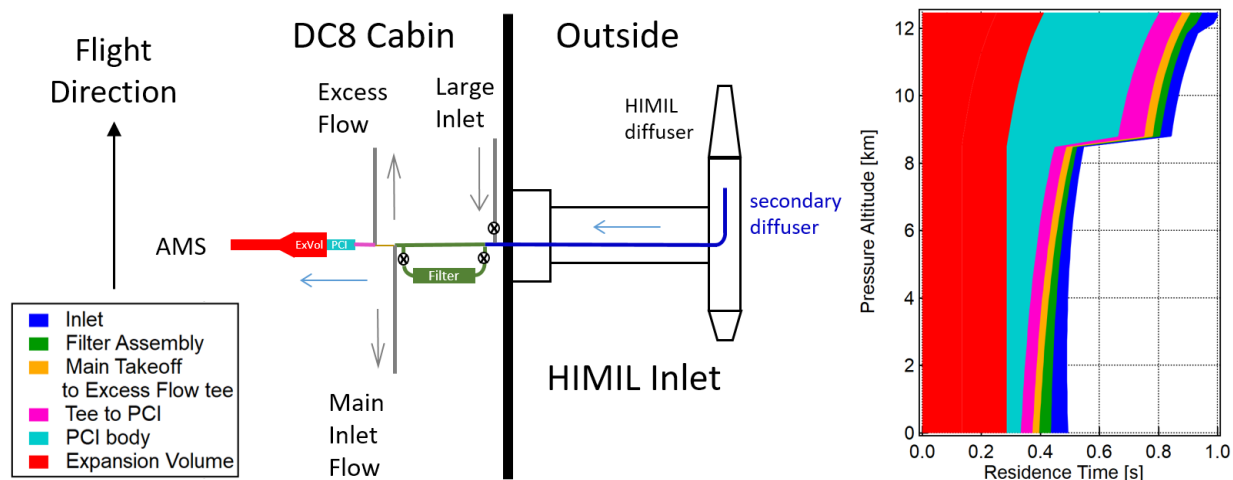


Fig. S3: Left: Simplified flow diagram for the AMS inlet assembly (not to scale, only the most relevant valves shown). Airflow is turbulent outside the cabin, and laminar inside. Air is pulled constantly through HIMIL at 9 sL min^{-1} up to $\sim 9 \text{ km}$ and 15 vL min^{-1} above that. The sum of AMS flow and excess flow is 2 vL min^{-1} controlled by two tandem critical orifices. Also shown is the line to the LARGE inlet operated by the AMP team that was used at times instead of the HIMIL to check performance (see the comparison in Fig. S5) (Brock et al., 2019). Right: Total residence time from the tip of the secondary diffuser inside the HIMIL to the AMS, as a function of altitude, color-coded by the different parts of the inlet assembly.

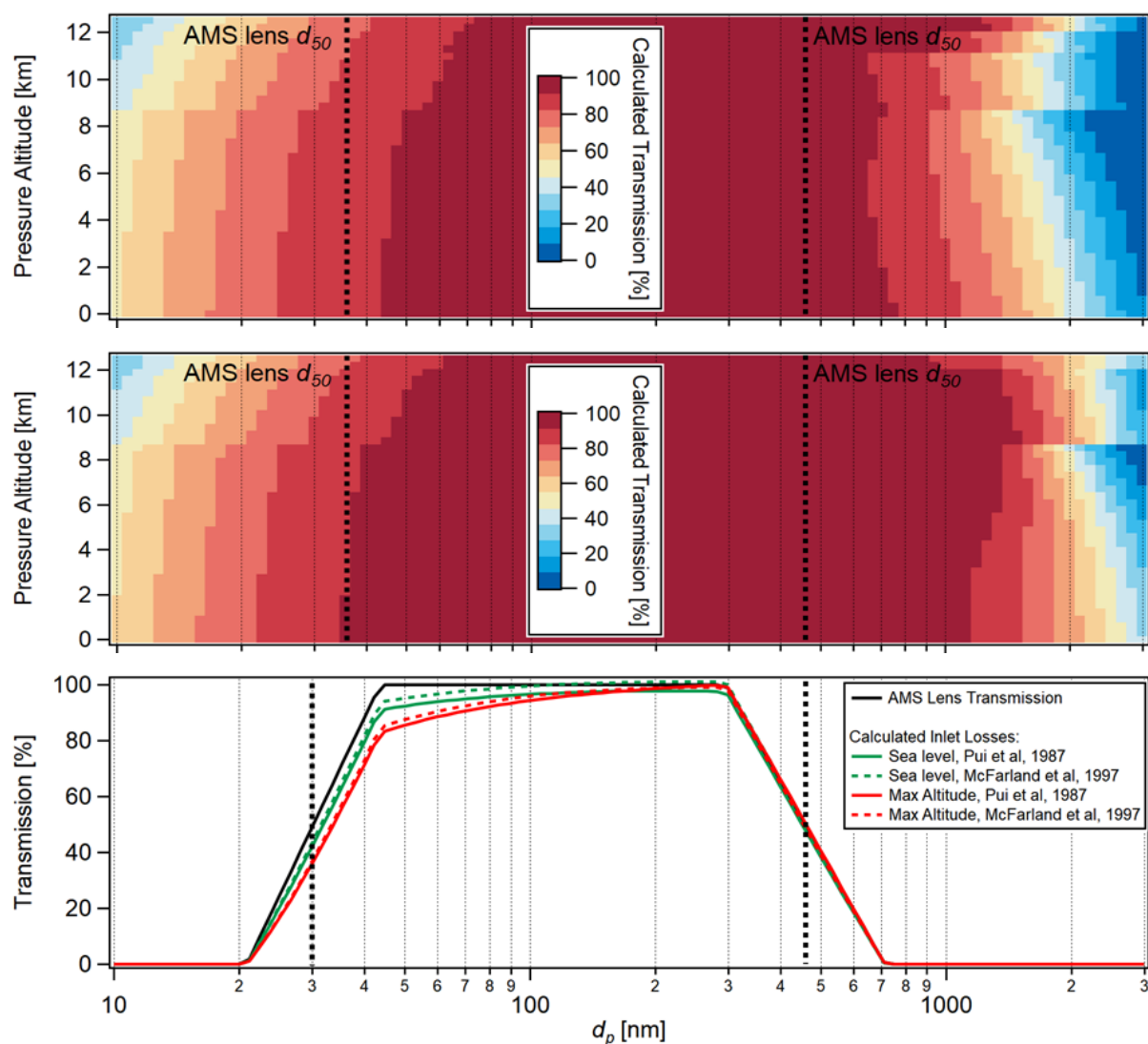


Fig. S4: Top: Calculated aerosol transmission through the AMS inlet plumbing for all ATom altitudes (including aerosol gravitational and diffusional losses and aspirational and inertial sampling efficiencies), assuming the average ATom1-2 mass-weighted density of 1.63 g cm^{-3} and using the Pui et al. (1987) parameterization of turbulent losses in bends. Middle: Same as top panel but using the turbulent loss formulation of McFarland et al. (1997) for describing losses in bends, which predicts higher transmission for intermediate Dean numbers. Bottom: Effect of these losses on the AMS transmission function at sea level and the highest ATom altitude, where the lower flows increase the losses due to diffusional deposition somewhat. Note that these transmission calculations do not include (a) the losses in the HIMIL inlet, which have not been fully characterized, but given the geometry likely has a d_{p50} of around $1\text{-}1.5 \text{ }\mu\text{m}$ (Porter et al., 1992;

Baumgardner and Huebert, 1993; Sheridan and Norton, 1998; Hermann et al., 2001), (b) the potential oversampling of large aerosols at altitude in the HIMIL secondary diffuser, and (c) the losses in the PCI. (c) is discussed in detail below (Fig. S6), (b) was not included in the calculations since there is scant experimental data on the validity of the parametrizations normally used for turbulent supersampling at higher Mach numbers (e.g., 0.2-0.4 under ATom conditions) and there is also limited data on what the actual flow speed inside the HIMIL is (slowdown by the primary diffuser is assumed to be about 3-4 times, D. Rogers, NCAR, pers. comm.). However, (a) and (b) were indirectly characterized by the comparison with the LARGE inlet, which does not include either of them and showed identical concentrations (Fig. S5).

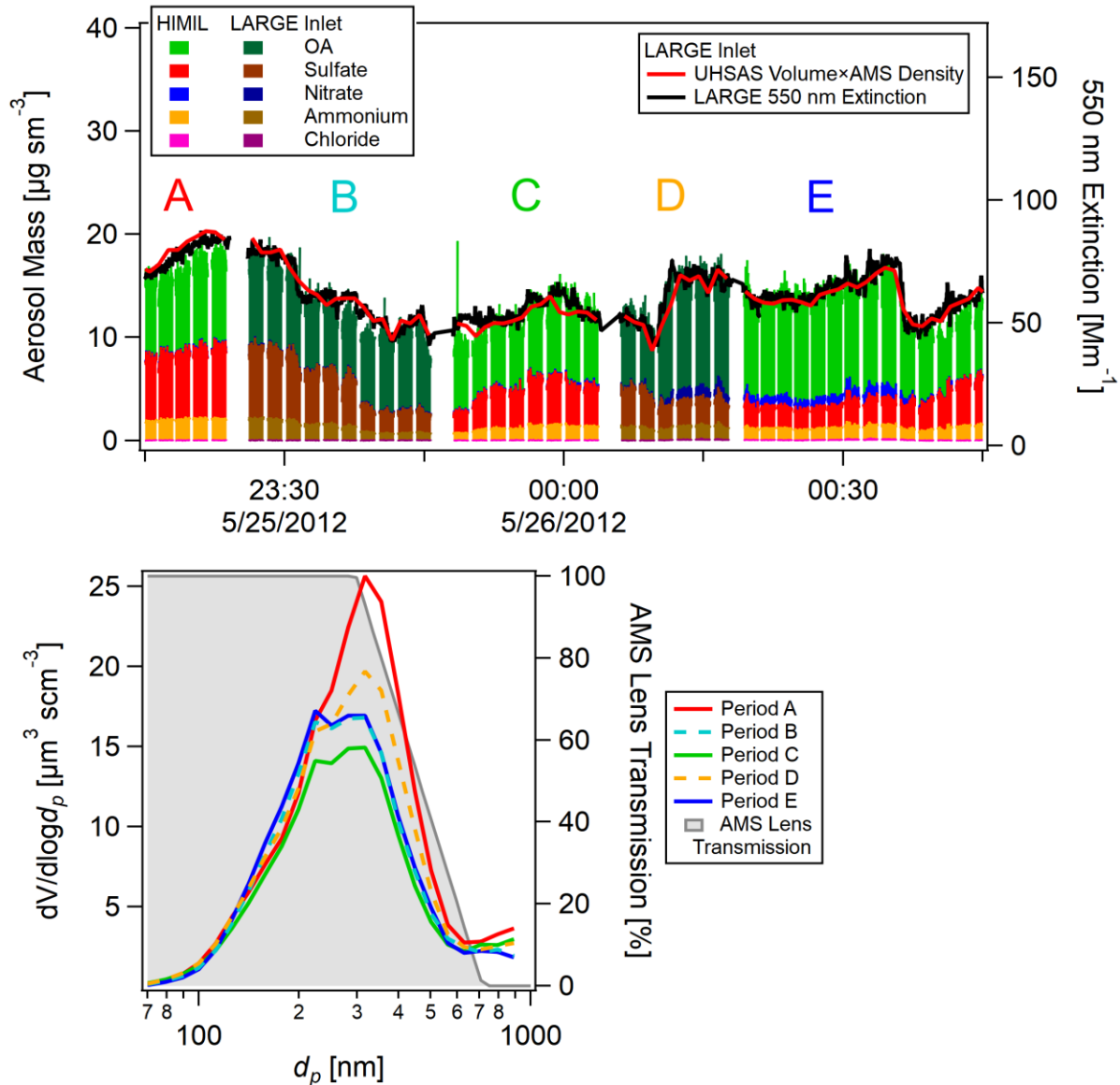


Fig. S5: Top: Comparison of AMS speciated mass with UHSAS volume (not corrected with the AMS transmission) and PM_{10} 550 nm scattering (both operated by the NASA Langley Group) for a period during Research Flight 4 of the NSF/NASA DC3 Mission (Barth et al., 2015), onboard the NASA DC-8, with the AMS sampling line being switched between the AMS HIMIL inlet and the LARGE inlet (the same inlet that the AMP Group used during ATom). Bottom: Average UHSAS volume distributions for the five periods shown. While comparisons like these were performed repeatedly during ATom with similar results, this one was chosen for illustration, due to the much higher concentrations and availability of concurrent optical measurements. The ATom-1&2 inlet transmission is also shown as an illustration since it was not fully characterized in the field during DC3.

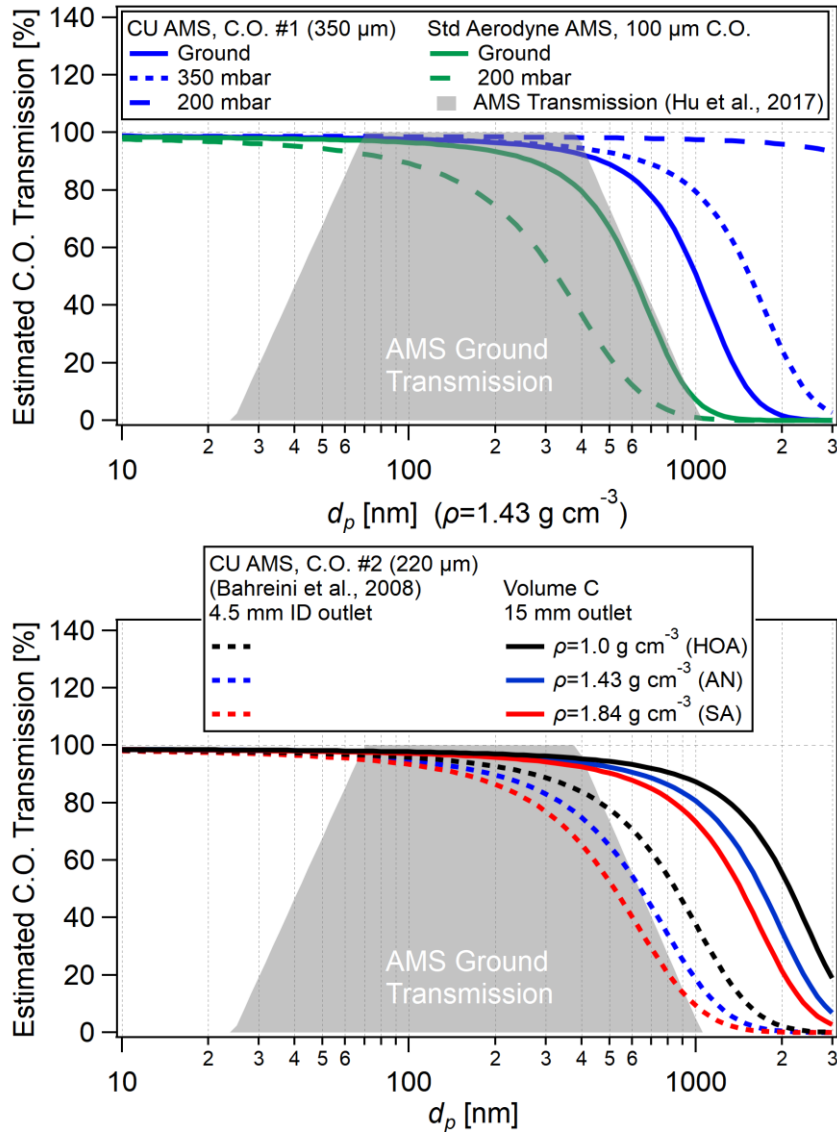


Fig. S6: Top: Calculated aerosol losses for ammonium nitrate aerosol (the standard AMS calibrant) for the CU AMS in the expansion behind the critical orifice (C.O.) facing ambient pressure (C.O. #1, top of the PCI), calculated for 3 different altitudes, based on a sigmoidal fit to the experimental data for the parametrization derived in Chen et al. (2007). Even at sea level, the losses are small compared to both the AMS transmission curve and the inlet plumbing losses. For comparison, the same calculation was performed for a standard AMS operating with a PM_{10} inlet (smaller orifice, smaller upstream diameter). A comparison with the published transmission curve for that instrument (Hu et al., 2017) suggests that in fact losses at the back of the C.O. are the main reason for the observed shape of the curve on the high end (losses at the front side are 1-2 orders of magnitude less for the sizes shown). Also shown is the performance of the same inlet at 200

mbar ambient pressure, suggesting major losses at low pressure/high sampling altitudes. Bottom: Same calculation for the bottom C.O. (C.O. #2, the one facing the AMS aerodynamic lens) of the CU AMS PCI. Three different aerosol densities are shown (Hydrocarbon-like OA, HOA; Ammonium Nitrate, AN and Sulfuric Acid, SA) to explore the impact of density on the overall transmission. Dotted lines show the transmission for a PCI geometry such as in Bahreini et al. (2008), with a ¼” tube behind the critical orifice, which leads to significant losses relative to the regular AMS transmission (the Volume A1 design had a similar restriction right after the expansion). Solid lines show the same calculation for an expansion volume of 15 mm diameter, as used in this work (see Volume C in Fig. S7, the diameter of the expansion fitting throat is used, i.e., the smaller side), showing much improved performance. It should be noted, however, that while these equations capture the trends well, the actual losses observed for these low pressures are significantly larger (see Fig. S9).

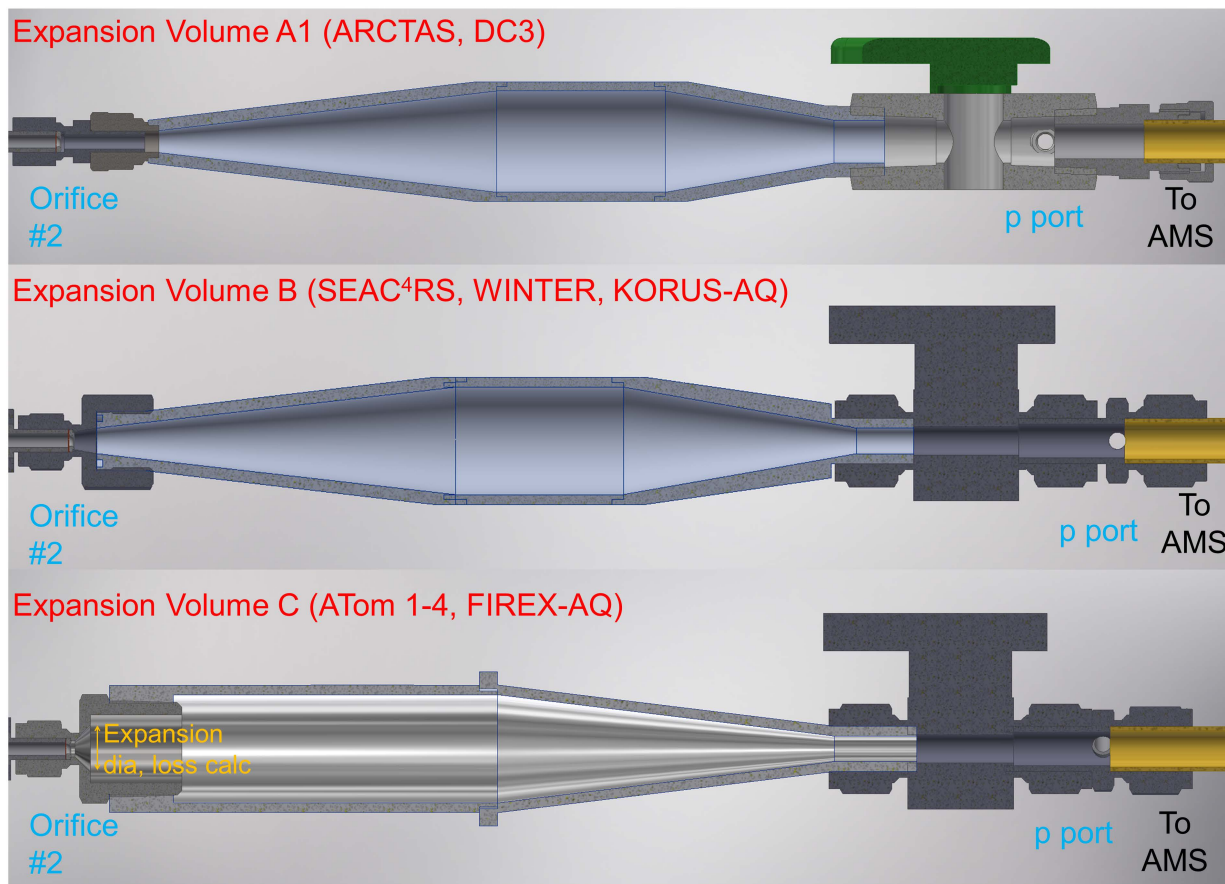


Fig. S7: Schematics of the three expansion volumes that have been flown with the CU AMS PCI over the past decade. Top: Initial design, based on computer fluid dynamics (CFD) calculations of X. Wang and P. McMurry (pers. comm.). This design includes a 7° conical expansion region behind the critical orifice, a 30 mm central section, and a 10° conical contraction region. The lens interface is identical to the standard PM₁ AMS Inlet (Zhang et al., 2004a; Canagaratna et al., 2007). The critical orifice was initially mounted as shown for the ARCTAS and DC3 missions (Jacob et al., 2010; Barth et al., 2015), which in some cases led to evaporation artifacts of ammonium nitrate calibration particles in the small tube immediately downstream of the orifice (Fig. S8). For part of SEAC⁴RS and the first five flights of the ATom mission, it was fitted with a new inlet similar to Volume B (referred henceforth as “Volume A2”), which ameliorated the evaporation artifacts during calibrations, but also for unknown reasons worsened performance at low pressure (Fig. S9). Middle: A redesign first flown during SEAC⁴RS (Toon et al., 2016), with the same inner dimensions as Volume A, but a) no obstructions behind the critical orifice and b) a new valve assembly with shorter overall length, more robust mounting and slight prefocusing of the aerosol

going into the aerosol lens, which should be beneficial for large particle transmission (Williams et al., 2013). While this volume exhibited no obvious evaporation artifacts, its performance at low pressure was significantly worse than Volume A (Fig. S8). It was used at higher pressure (430 mbar) for the WINTER and KORUS-AQ deployments that had a clear lower tropospheric focus. Bottom: For ATom, a new expansion volume C was designed for ATom on the assumption that a rapid expansion post-orifice at the highest possible angle is preferable. The focusing diffuser angle was reduced to 7° , which should minimize losses. The rest of the design is similar to Volume B.

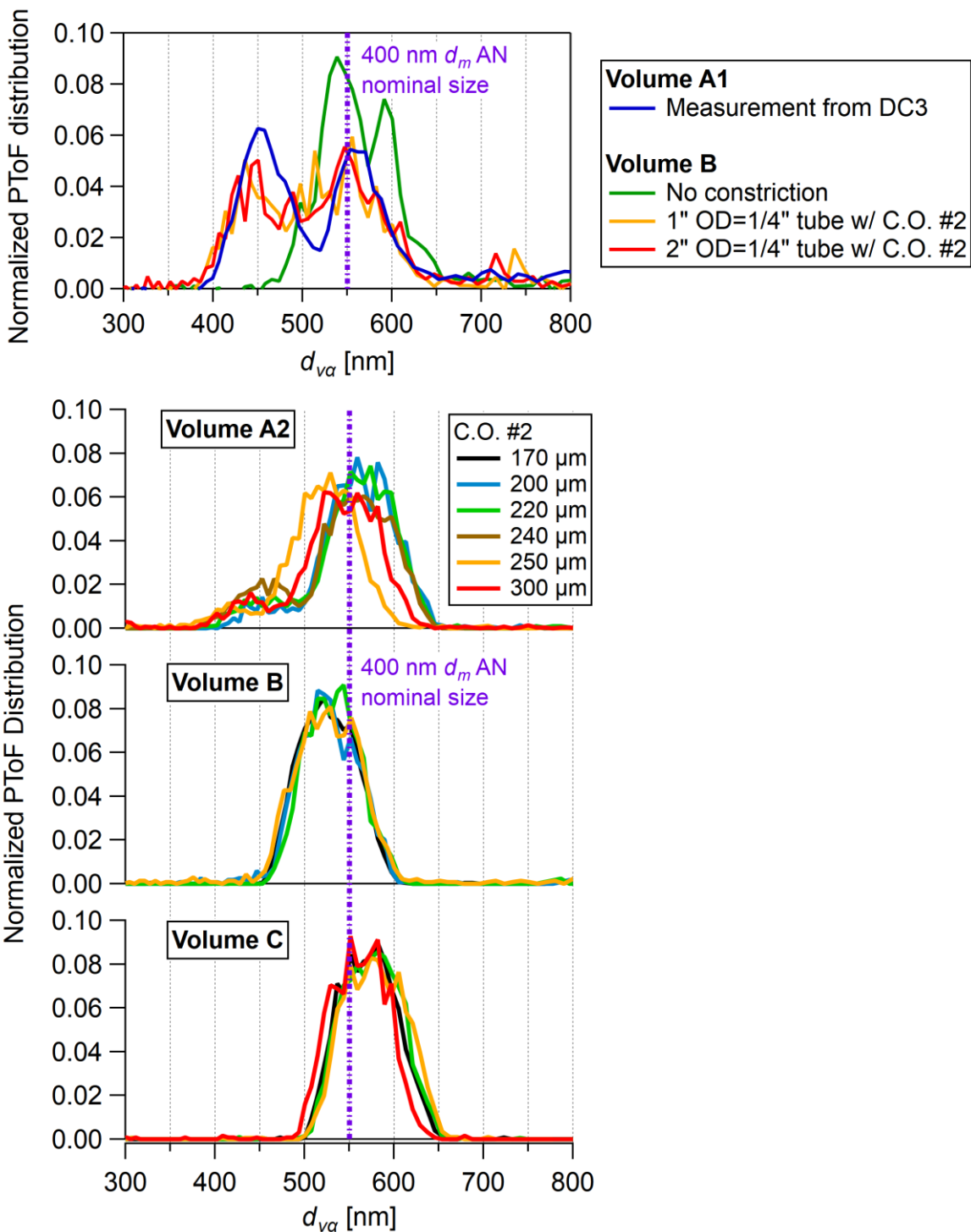


Fig. S8: Top: Evaporation artifact for ammonium nitrate calibration particles observed for Volume A and its cause: Sampling ammonium nitrate with Volume A shows a clear bimodal distribution, with the main peak significantly shifted down from the nominal aerosol size, indicating evaporation/shattering. For Volume B, this artifact is normally not observed, but can be induced

by inserting different lengths of ¼" OD tubing behind the critical orifice mount, mimicking the geometry in Volume A. Bottom 3 panels: Comparison of the size distributions observed for all three volumes during ATom (e.g., after the inlet of Volume A was replaced), again when sampling monodisperse 400 nm (d_m) ammonium nitrate aerosol. Volume A still exhibits an evaporation artifact, though considerably smaller. While no bimodal distribution is observed for Volume B, a slight shift of the main distribution is still apparent. Volume C does not show any of these issues, except possibly at the lowest pressure.

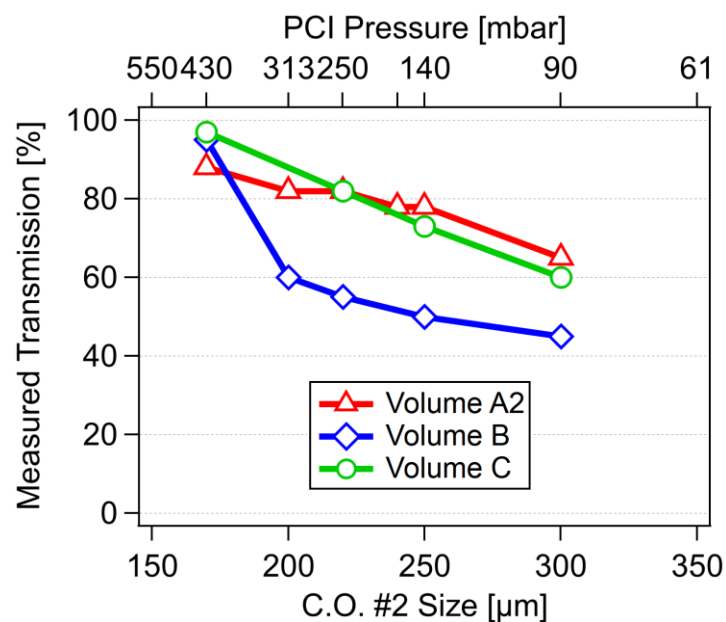


Fig. S9: Intercomparison of the performance of the three expansion volumes shown in Fig. S7 as a function of PCI pressures (and corresponding C.O. sizes). Monodisperse 400 nm (d_m) ammonium nitrate aerosols were used, and the transmissions were determined by Event trigger/CPC comparison, as done for the derivation of the lens transmission described in the main text. It should be noted that to cover the full altitude range of the DC-8, without losing sampling flow into the AMS, an orifice size of at least 250 μm and a PCI pressure of 135 mbar is needed. All volumes perform well at 430 mbar, roughly comparable to the Bahreini et al. (2008) published data at 467 mbar. For reasons that are still unclear, Volume B performs poorly below that pressure, while for both Volume A and C a more gradual loss in transmission is observed. For ATom operation, Volume C was operated at 250 mbar (220 μm C.O.), as a compromise between good transmission at lower altitudes and some AMS airflow loss at max altitude.

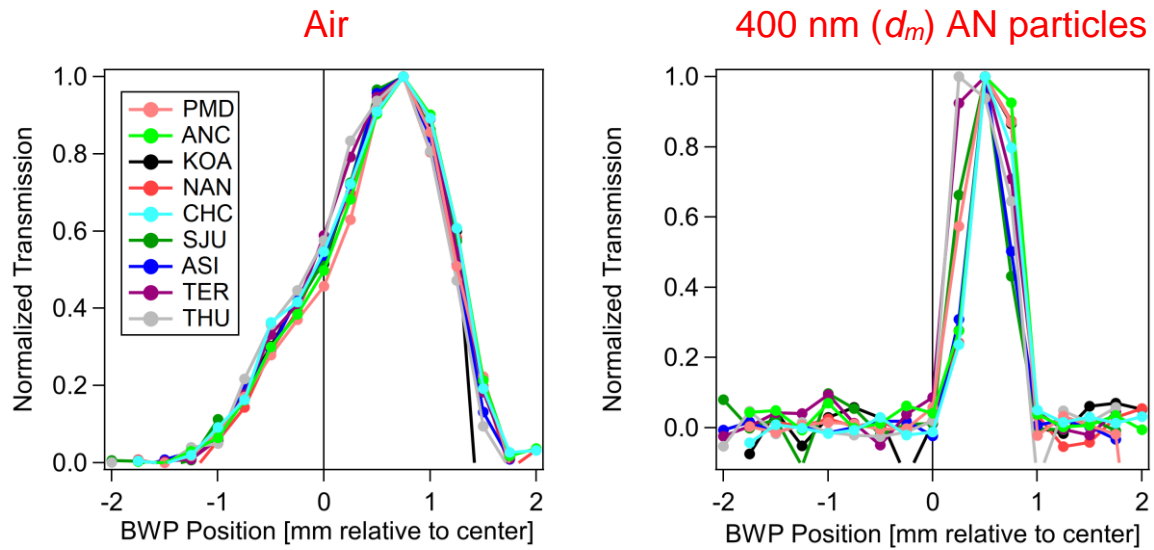


Fig. S10: Profiles of the AMS air beam (left) and particle beam (for monodisperse 400 nm ammonium nitrate particles) recorded at the entrance of the AMS ionizer with a beam width probe (BWP) (Huffman et al., 2005) over the course of ATom-2 (Legend indicates the ICAO code for the airport the profiling was performed). This was a standard calibration taken at the end of most flights during ATom and served as confirmation that no lens misalignment had occurred.

5. AMS composition-dependent CE

Composition-dependent CE calculated based on Middlebrook et al. (2012) was applied to the AMS quantified mass and was near 1 most of the time, a consequence of the high acidity of the ATom observations. A possible deviation typically originates from external mixtures, such as fresh primary organic aerosol (POA) or nitrate plumes, as in some urban environments. The contribution of POA is very small for the aged and remote aerosols sampled during the ATom (Hodzic et al., 2020). In the ATom context, the two main sources of uncertainty in this area are externally mixed sea salt plumes in the marine boundary layer, and possibly externally mixed OA newly formed in the upper troposphere (Williamson et al., 2019). The latter effect is ruled out due to not observing an altitude-dependent deviation in the volume closure, despite the fact that the Aitken mode contributed up to 50% of the mass in the upper troposphere. In the current manuscript, we have always assumed sea salt to be externally mixed and assumed a $CE=1$ in the moist boundary layer. It is important to note that the uncertainties in size cut, effective density, and RIE of sea salt are likely larger than the uncertainty in CE for sea salt aerosols. Overall, for the intercomparisons presented in this study, we don't observe a deviation correlating with a potential CE effect, thus concluding that such deviation is within the reported 30% uncertainty of CE .

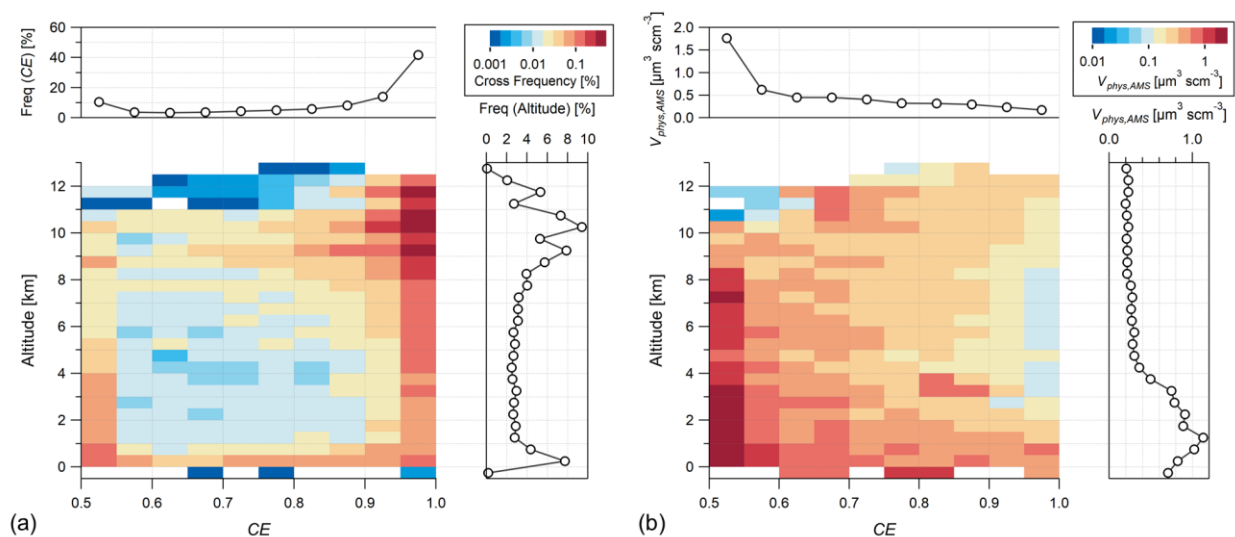


Fig. S11: Frequency distributions of composition-dependent CE and altitude for ATom-1 to -4 studies: the left panel colored by the cross frequency of CE and altitude and the right panel colored by $V_{phys,AMS}$. The composition-dependent CE is applied to all AMS mass products except for sea

salt, that is likely externally mixed with the other components. A *CE* of 1 is assumed for sea salt in the moist boundary layer.

6. AMS in-field calibrations

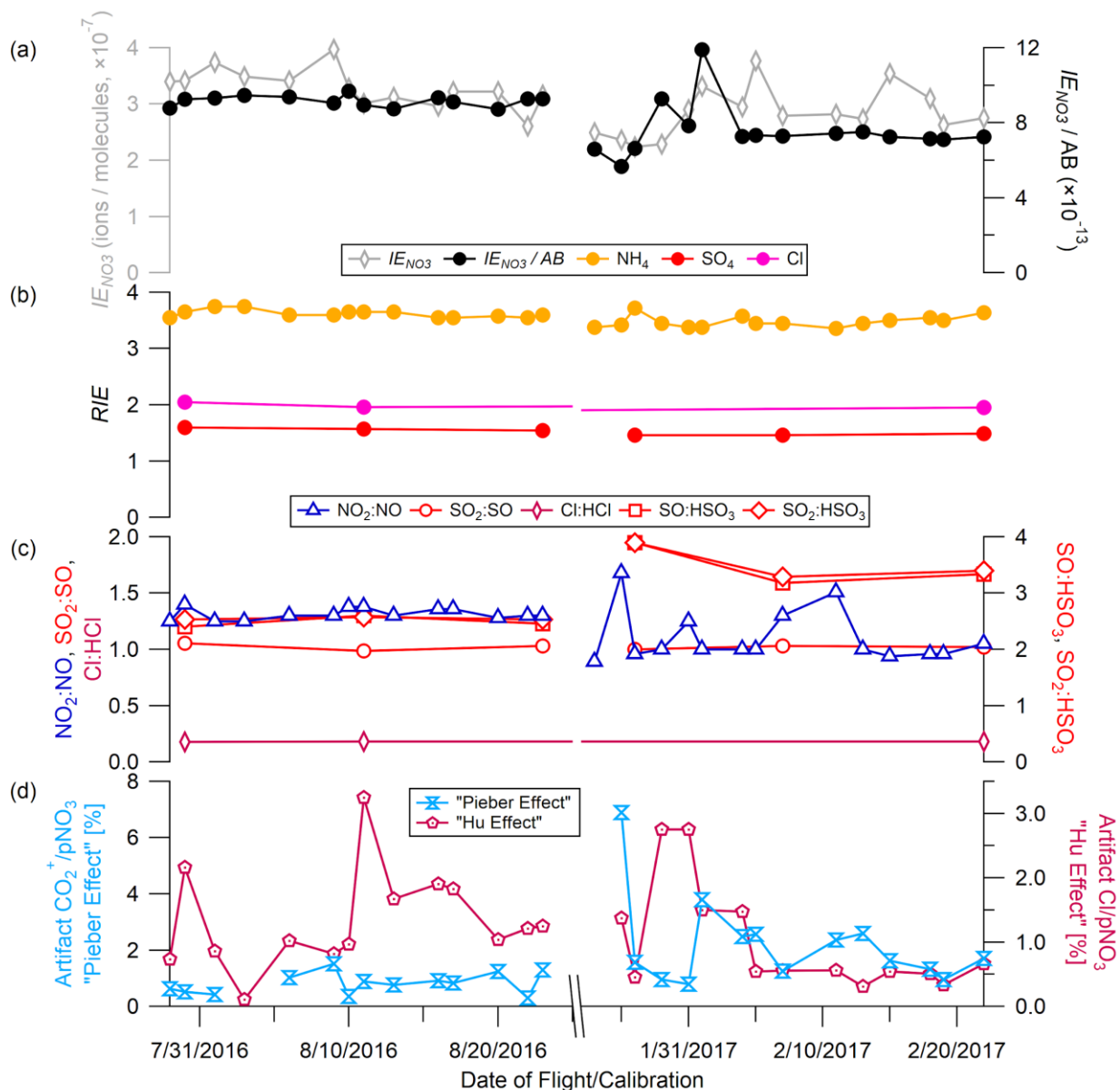


Fig. S12: Time series of results from in-field calibrations in ATom-1 and -2 for (a) the ionization efficiency of nitrate (IE_{NO_3}), IE_{NO_3}/AB (air beam); (b) the relative ionization efficiency (RIE) for ammonium (NH_4), sulfate (SO_4), and chloride (Cl); (c) the ion ratios; (d) the measured artifact signal ratios for CO_2^+/pNO_3 "Pieber Effect" (Pieber et al., 2016) and Cl^+/pNO_3 "Hu Effect" (Hu et al., 2017). The most critical calibrations were performed immediately after each flight. The 2σ uncertainties of RIE_{NH_4} , RIE_{SO_4} , and RIE_{Cl} are 4% (6%), 4% (2%), and 5% (8%), respectively for ATom-1 (ATom-2), all smaller than the reported values from (Bahreini et al., 2009). The 2σ uncertainty of the ionization efficiency (normalized as its ratio to the air beam signal, IE_{NO_3}/AB) is

6% for ATom-1 and 15% for ATom-2 (excluding the two large numbers measured on Jan 29 and Feb 1, 2017; if averaging after Feb 1, the uncertainty drops down to only 4%, showing that the AMS ionization efficiency performance became very stable for the latter two-thirds of the ATom-2 deployment after the unstable start).

7. PALMS relative data coverage for ATom conditions

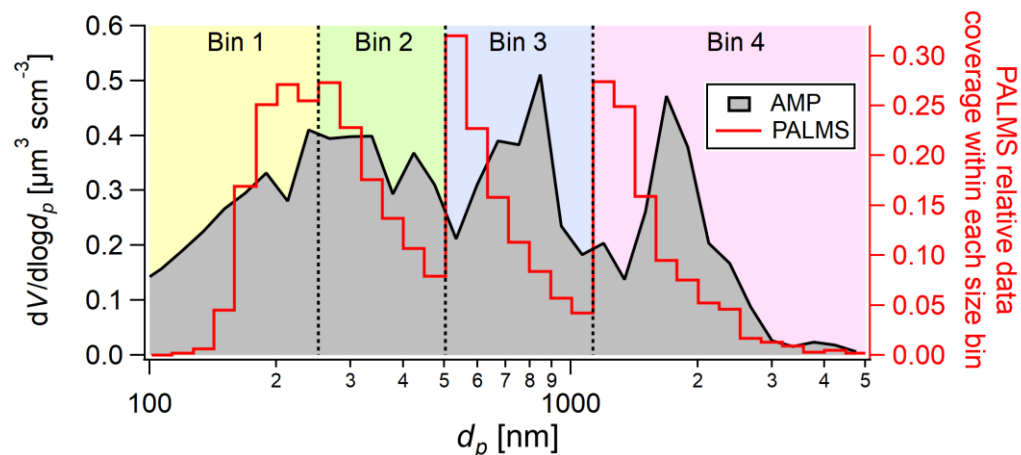


Fig. S13: PALMS composition coverage across the accumulation and coarse modes (K. Froyd, pers. comm.). For ATom-2, the AMP size distribution (black line, campaign average) is divided into 4 bins. The PALMS fractional composition data is calculated as an unweighted mean within each bin. The red solid line shows the PALMS relative data coverage within each bin, showing variation in relative coverage within each bin. For example, in the smallest bin (Bin 1), the PALMS composition means will be weighted to sizes >140 nm. If the aerosol composition is homogeneous within each bin, this uneven composition coverage by PALMS introduces no bias. Actual biases were quantified in Froyd et al. (2019) using atmospheric data.

8. PALMS detected particles and the operational size coverages for the PALMS-AMP derived aerosol compositions

For intercomparisons, we characterize the specific size range over which the PALMS can obtain sufficient aerosol chemical composition over a given time period under the ATom conditions, which is mainly limited by particle statistics. If zero or a very low number of particles is sampled for a given AMP size bin and time period, there is no real information being captured for characterizing the composition of the particles in that bin. That is true even if the AMP volume in that bin is assigned a composition by extrapolating the composition of larger or smaller particles. Therefore, we derived the PALMS detected particle numbers based on the raw AMP size resolution (20 bins/decade, 34 bins in total above 100 nm d_p for the size range that PALMS-AMP reports) to avoid the assumption of homogeneous chemical composition within four broader bins in Froyd et al. (2019). The method is straightforward by apportioning the sum of reported PALMS detected particle numbers (in the positive mode) into each size bin with the detection efficiency curve (Froyd et al., 2019). Sufficient size resolution is important to characterize ambient particle composition, which can at times be highly size-dependent (Zhang et al., 2004a), and when analyzing phenomena with strong nonlinear transitions such as cloud condensation nuclei (CCN) activation. Note that we are not arguing that the reported PALMS data products should be changed or processed differently. Instead, we are characterizing the operational size coverage of PALMS and comparing it to other aerosol instruments. This provides an alternative illustration of PALMS size coverage and introduces a method that is applicable to other single-particle mass spectrometers or other particle-counting-based chemical instruments.

The estimated PALMS detected particle numbers across the size range generally agreed with the data posted as the comment by the PALMS team (Murphy et al., 2020) (Fig. S14). Importantly, we applied a 0.64 scaling factor to the PALMS team curve which accounts for both positive and negative mode spectra since the main mass products, such as OA and SO₄, were derived based on the positive spectra only (Froyd et al., 2019) (N_{pos} was slightly larger than N_{neg} during ATom). The largest discrepancy is found at 130 nm with a ratio of 4.5 suggesting an underestimation of our method in Bin 1 (100-240 nm d_p). As a sensitivity test, we moved the detection efficiency curve 10 nm smaller for Bin 1 and got this ratio down to a value consistent with the other bins. The 10 nm is within the reported uncertainty of detection efficiency curve in Fig. 6 in Froyd et al. (2019). This figure also shows that the curve (only for ATom-1) can change

with altitude, particle composition, inlet performance, and unknown factors between different cases. Additionally, the effects of software or hardware limitations were not considered. So most of the difference between our estimation and that posted by the PALMS team can be explained by how well the detection efficiency represents the actual counts and the size uncertainties. In the following analysis, we use the slightly shifted PALMS detection efficiency curve to estimate detected particle numbers as the most accurate evaluation based on the publicly available data (as shown in Fig. S14b).

The PALMS detected particle curve appears to be an inverted U-shape. For the small particle end (< 200 nm in Fig. S14), the very sharp decrease in the PALMS detection efficiency curve (Fig. 6 in Froyd et al. (2019)) dominates over the increasing atmospheric particle concentrations at smaller sizes reported by AMP. For the large particle end (> 2.5 μm), fewer large particles were present in the air despite the slight increase in the PALMS detection efficiency curve at larger sizes.

The 20 bins/decade size resolution of AMP is preferable as it makes the results directly comparable to the other aerosol instruments. Also, it shows the possible variability within a broad size bin. In Fig. S15, the probability of detecting on average one valid particle per AMP size bin in the PALMS is very low below ~ 160 nm and above 1000 nm over a typical 3 min analysis period. Fig. S15 also plots several other size resolutions to illustrate the effect. The 20 bins/decade curve is not much different from 10 bins/decade or 40 bins/decade, and they share a similar overall profile. The 5 bins/decade curve is on the same level as the PALMS 4 bins but both smooth out the variabilities on a finer scale. While holding the size resolution at 20 bins/decade, better counting statistics can be reached by averaging over a longer time period (Fig. S15).

As altitude increases in the free troposphere, the size distribution often shifts to smaller diameters (Williamson et al., 2019), thus we expand the 1D profile in Fig. S15 to include the altitude dependence (Fig. S16). The results are shown at 3 min, 60 min intervals, as well as campaign-wide. The 3 min timescale is most relevant for high time resolution airborne analyses (~ 36 km horizontal distances and ~ 1.5 km ascent/descent distances under the typical ATom flight profile) while the longer ones are relevant to averages by altitude in a latitude band and similar analyses that group data together from different time periods.

Since Froyd et al. (2019) require ≥ 5 particles in each (broad) size bin to have good counting statistics, we assume that if PALMS detects one particle in a given AMP size bin, the composition

of the bin is fully characterized. The two criteria are similar: the 4 bins with ≥ 5 particles mean in total 20 particles, while the AMP-size-resolution-based analysis means in total 35 particles (for the 35 size bins). Please note that, the chosen criterion in this study is simply adapted from Froyd et al. (2019) to analyze the operation size range of PALMS during ATom studies. In reality, more particles might be required to fully characterize the particle composition for a narrow size bin at the higher size resolution for the possible existence of externally mixed aerosols or the variations of internally mixed aerosols. However, this conservative scaling implicitly acknowledges some degree of correlation between the higher-resolution bins. Then, we take the PALMS detected particle number in each size bin to approximate the size ranges observed by PALMS, assigning 100% “transmission” when the PALMS detected particle number is above 1.

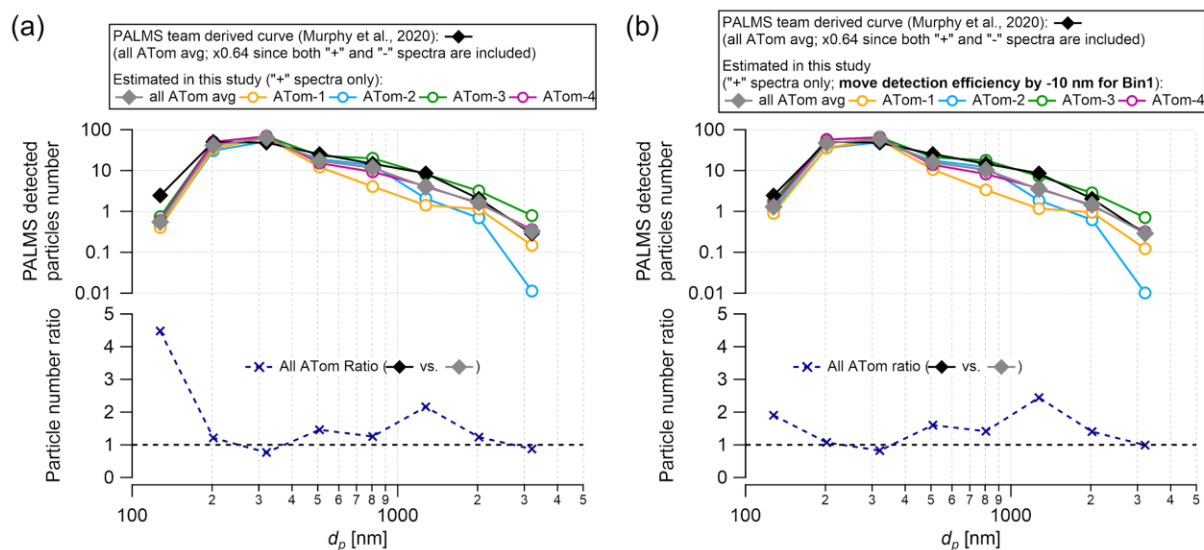


Fig. S14: (a) Comparison of the PALMS detected particle numbers over 3 mins time interval between Murphy et al. (2020) and the estimates in this study based on the original ATom-1 PALMS detection efficiency curve in Fig 6 of Froyd et al., (2019). The data are shown at a resolution of 5 bins/decade, for consistency with Murphy et al. (2020). The bottom panel shows the ratio between the two methods. (b) Sensitivity tests by moving the PALMS detection efficiency 10 nm smaller for Bin 1 (100-240 nm; thus leading to higher particle counts in this size range), all else stays the same. The 10 nm is roughly the reported uncertainty of the PALMS detection efficiency curve, while the actual uncertainty is probably larger when considering the limitations in software or hardware.

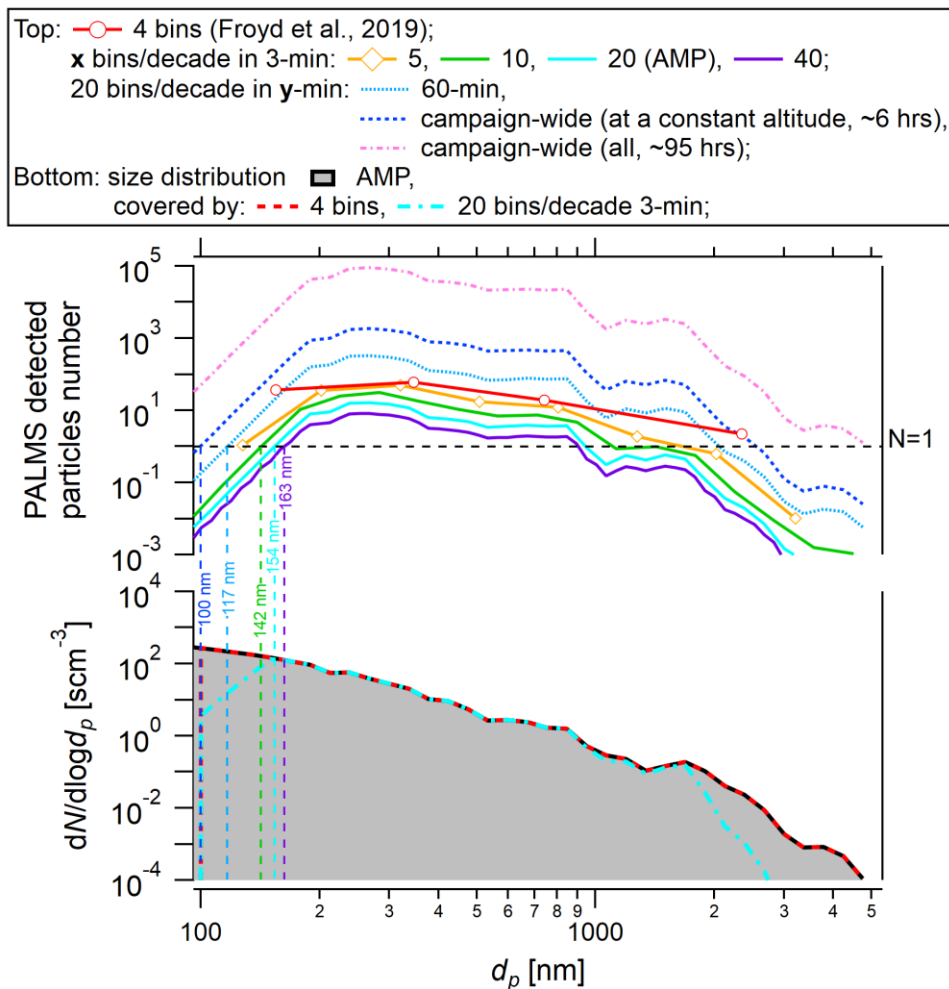


Fig. S15: (Top) PALMS detected particle numbers per size bin at several size resolutions at a 3-min time interval (i.e., the time resolution that the public PALMS-AMP mass products are reported at) and longer averaging time scales for ATom-2. (Bottom) The ATom-2 campaign averaged AMP number size distributions with the fraction that is characterized by PALMS-AMP.

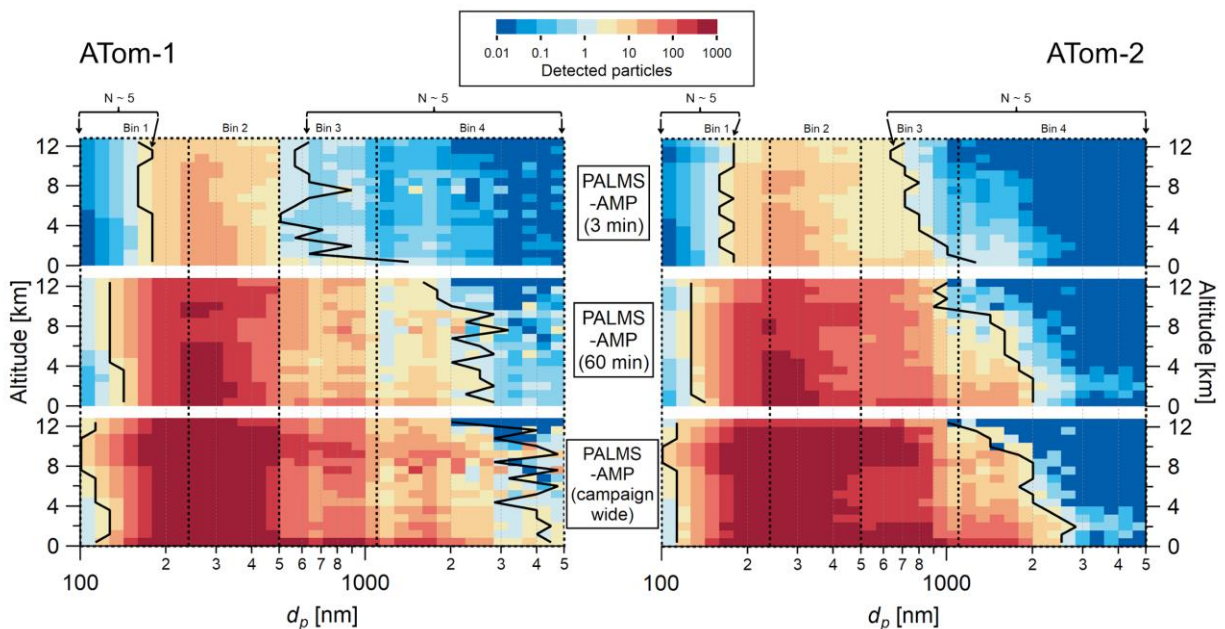


Fig. S16: Altitude dependent PALMS detected particles during a 3-min (top), 60-min (middle), and campaign-wide (bottom) averaging time scale for the conditions in ATom-1 (left) and ATom-2 (right). Dashed rectangle areas represent the 4 larger bins used for the 3-min PALMS-AMP product (Fig. S13). The solid black lines represent the minimum size ranges to have 5 particles (consistent with Froyd et al. (2019)) detected for the range between 100 nm and the left black line, or between the right black line and the upper size limit of AMP.

9. SAGA MC inlet design

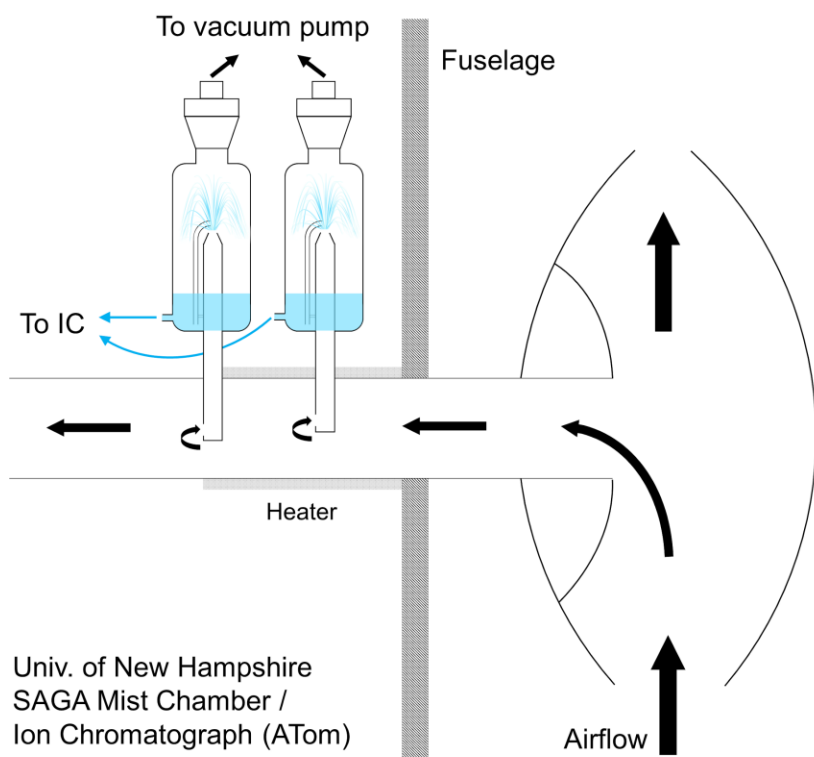


Fig. S17: Schematic diagram of SAGA MC IC during ATom.

10. SAGA MC inlet transmission

van Donkelaar et al.(2008) estimated the cutoff size to be $\sim 1 \mu\text{m}$ ($d_{ta,sea}$) for SAGA MC. Due to the lack of an available SAGA MC inlet transmission profile from literature, we take the MOUDI $1\mu\text{m}$ stage impactor transmission (discussed in Sect. 3.2 in the main text; Fig. S24) as an approximation to evaluate the change in SAGA MC d_{50} (particle diameter with 50% transmission) as DC-8 climbs. P , T , and air velocity affect d_{50} . During ATom, the P effect is the same for SAGA MC as compared to MOUDI since the two inlets operate at ambient P . The other two effects make the SAGA MC d_{50} differ from the MOUDI d_{50} . First, the T of MOUDI impactor airflow is assumed to be the cabin T (293 K) (Guo et al., 2016), while the T of SAGA MC air flow is assumed to be the outside ambient T (as discussed in the main text). Second, the air velocity in the SAGA MC manifold is expected to increase with altitude, leading to further shift of cutoff size to smaller sizes. In contrast, MOUDI has a choked airflow of 30 L m^{-3} . Here, we take the SAGA MC airflow as an approximation to estimate the change in the manifold airflow (only the ratio of air velocity matters in this calculation), since the vacuum of both was provided by venturi pumps. The SAGA MC airflow increased linearly below 10 km and stayed nearly constant above that (Fig. S18b).

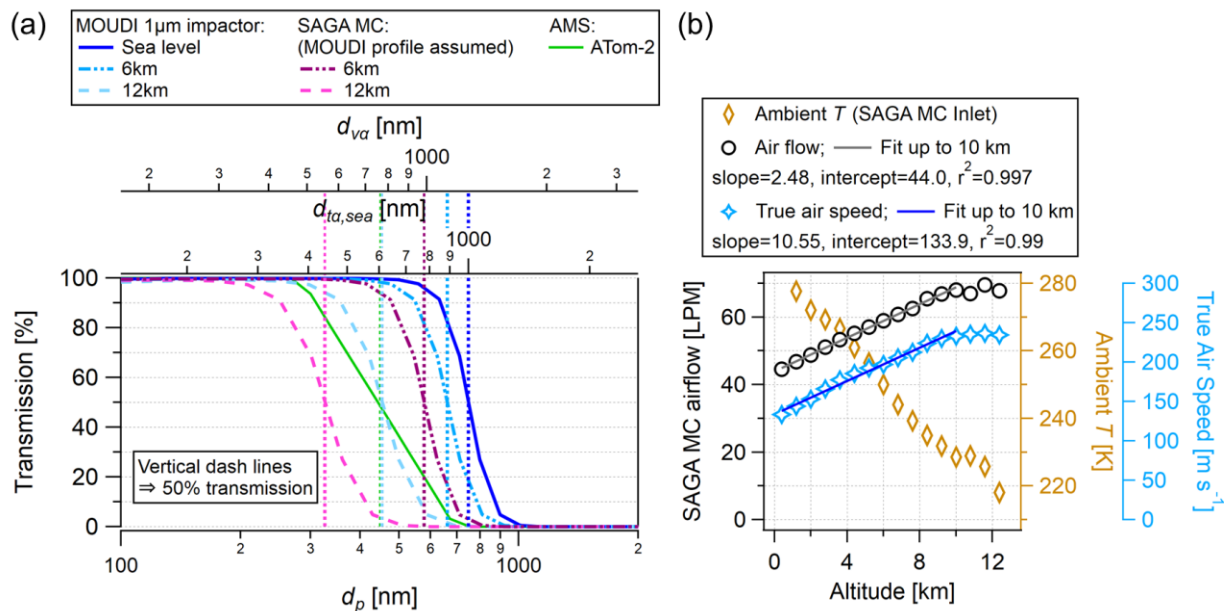


Fig. S18: SAGA MC inlet (a) transmission (compared to the MOUDI 1µm stage impactor and AMS), (b) airflow, outside ambient temperature, and true air speed of DC-8. Note that the SAGA MC transmission is assumed with the MOUDI transmission profile to investigate the altitude dependency. The SAGA MC and MOUDI transmissions are displayed at sea level (STP), 6 km, and 12 km (P based on the U.S. standard atmosphere for both; ambient T for SAGA MC inlet and cabin T for MOUDI) (NOAA, NASA, U. S. Air Force, 1976). In contrast, the AMS transmission is valid up to ~9 km and a similar performance is expected at the max altitude. The conversions between d_p , d_{ta} , and d_{va} are based on the ATom-2 dry aerosol density of 1.70 g cm⁻³. A complexity of SAGA MC d_{50} is not considered for this plot, as the SAGA MC inlet size-selects particles at ambient conditions (i.e., particles with liquid water if deliquesced) while the MOUDI inlet size-selects dry particles (Guo et al., 2016). This effect is larger below 3 km, where ambient RH was higher (75% to 40%, from the surface to 3 km), and minimal above 3 km, where ambient RH was on average below 40%. So the plotted 6 km and 12 km SAGA MC d_{50} are fairly accurate.

11. SAGA filter inlet transmission

The transmissions for large particles are based on the UNH inlet transmission, Fig. 8C in McNaughton et al. (2007), and adjusted to the ATom conditions, ρ_p of 1.7 g cm^{-3} and true air velocities of DC-8. For the coarse mode, the transmissions would shift when the ρ_p of 1.7 g cm^{-3} (estimated for submicron) do not represent some pure dust plumes with a density of 2.5 g cm^{-3} or sea salt plumes with a density of 1.45 g cm^{-3} (Froyd et al., 2019). While particles were size-selected at ambient conditions (i.e., with particle liquid water), we apply the transmission to AMP dry particle size distribution without considering the effect of particle water on size. The bias with this simplification is small for less hygroscopic coarse particles (i.e., dust) and large for more hygroscopic particles (i.e., sea salt) (Kumar et al., 2009a, 2009b; Nenes et al., 2014). Furthermore, the bias is larger below 3 km, where ambient RH was higher and decreased from 75% to 40% (surface to 3 km), and smaller above 3 km, where ambient RH was on average below 40%. The diffusion losses (turbulent regime) for small particles are estimated for an approximate 140 cm sample line tubing with an inner diameter of 5 cm (more accurate inlet dimensions discussed below), for which 100 cm are outside of the plane (ambient T) and the rest 40 cm are inside. Here we take the average of ambient T and a typical cabin T of 293 K due to the high air flow of SAGA and the use of Delrin material for most of the in-cabin sample line, which doesn't conduct heat as well as the steel inlet. Note that, using ambient T to estimate the diffusion loss only results in 0.7% lower transmission at the minimum particle size of $2.67 \text{ nm } d_p$, i.e., 79.4% vs. 80.1%). The dimensions of the SAGA filter inlet are as follows. The UNH diffuser-type inlet tip was designed with shrouds (McNaughton et al., 2007). It extends inside of the cabin only 5 cm before it is connected to a large ball valve, $\sim 10 \text{ cm}$ long, with the same inner diameter as the inlet tube. Downstream of the ball valve, a diffuser, $\sim 20 \text{ cm}$ long, expands from 5 to 9 cm just before connecting to the filter holder (filter diameter is 9 cm). Both the ball valve and diffuser are made of Delrin. The collection efficiency of the Zefluor filter ($1 \text{ }\mu\text{m}$ pore size) that SAGA uses is not estimated because Zíková et al. (2015) find it to be significantly underestimated by theoretical calculations and requires in-lab characterization.

Aspiration efficiency is the ratio of the number concentration of particles that enter the sampling probe to that in the ambient air. Here, we estimate the efficiency with Eq. 5 in Weiden et al. (2009) (Belyaev and Levin, 1972, 1974) and the inlet tip internal diameter of 7.77 mm (McNaughton et al., 2007). The range of validity for this equation is shown as the two dashed

curves in panel (b) of Fig. S19 due to the Stokes Number. In general, the aspiration effect is less for small particles vs. large particles, and large particles are sub-sampled at low altitudes (< 8 km) and over-sampled at high altitudes (> 8 km). Due to the very limited range of equation validity and the fact that both the nozzle air velocities (120-333 m s⁻¹) and true air velocities (133-234 m s⁻¹) are above the recommended limit of the equation, 30 m s⁻¹ (von der Weiden et al., 2009), the aspiration efficiency is not applied to the SAGA filter inlet transmission.

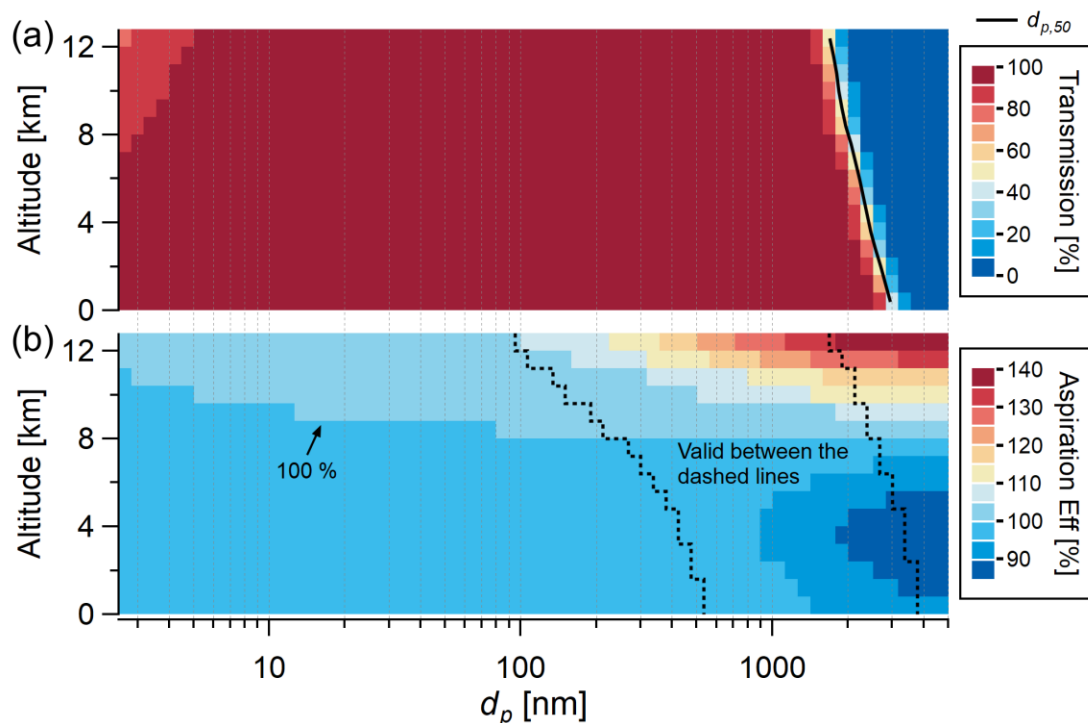


Fig. S19: SAGA filter inlet transmission (a) and aspiration efficiency (b) plotted with d_p and altitude during AToms.

12. Aerosol density and OA density

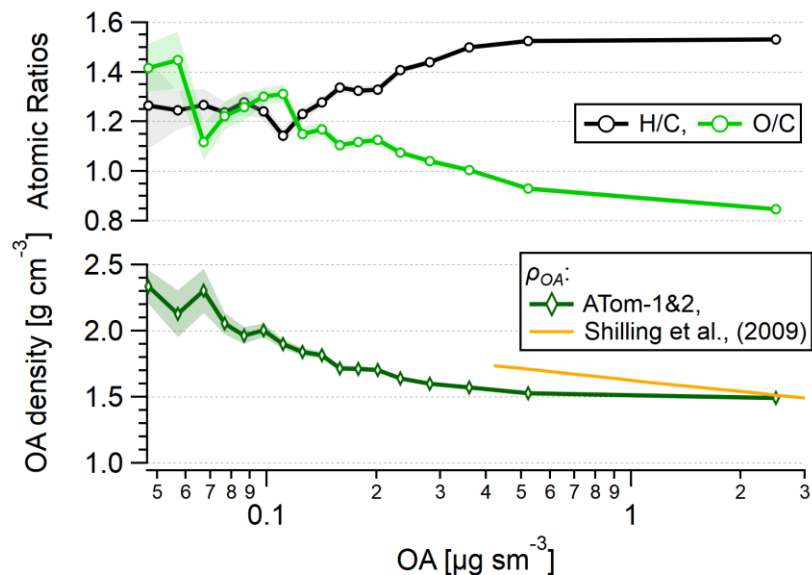


Fig. S20. The ATom-1&2 OA atomic ratios (H/C, O/C) and density vs. concentration. The shaded regions represent the precision as a standard error. This figure shows an increasing trend of ρ_{OA} at lower OA mass concentrations. As Fig. S21 shows high ρ_{OA} , such as 2.0-2.3 g cm^{-3} , is only predicted for a small percentage of the data points. Also shown is a similar trend of increasing density vs. mass loading, with similar values for the same OA concentrations, previously reported in laboratory SOA studies (Shilling et al., 2009).

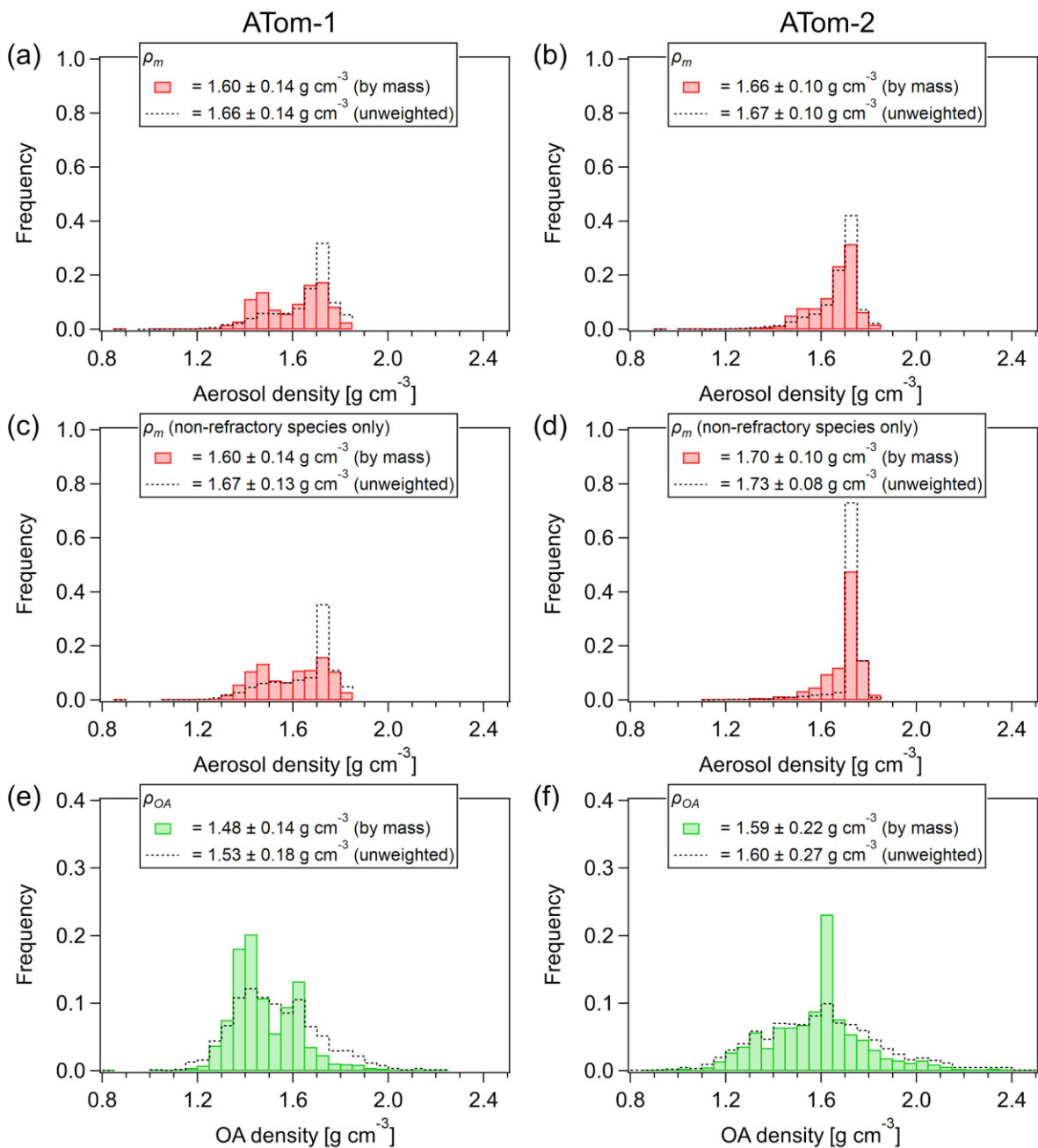


Fig. S21: Frequency distributions of dry aerosol density (ρ_m) and OA density (ρ_{OA}) for ATom-1 (left) and ATom-2 (right). The ρ_m in the top panel a&b is calculated via Eq. 5 in the main text and the ρ_m in the middle panel c&d excludes the refractory species rBC and sea salt. Excluding rBC and sea salt in the aerosol density calculation changes the ρ_m averages within 0.01 g cm^{-3} for ATom-1 and 0.04 g cm^{-3} for ATom-2. When OA is below DL, ρ_{OA} is excluded due to the large

uncertainties in the ρ_{OA} estimation. Both the mass-weighted and the unweighted density campaign averages are plotted. Lower mass concentrations were associated with more aged conditions and more oxidized OA, and thus higher densities. As expected, the unweighted density is higher than the mass-weighted one. High ρ_{OA} , such as 2.0-2.3 g cm⁻³, is predicted for a small percentage of the data points, as the tail of the frequency distribution. The noise in H/C and O/C broadens the distributions of ρ_{OA} and the effect can be reduced by averaging to a longer time scale than the 1 min time resolution shown here.

13. Dust contribution to aerosol volume in the AMS size range

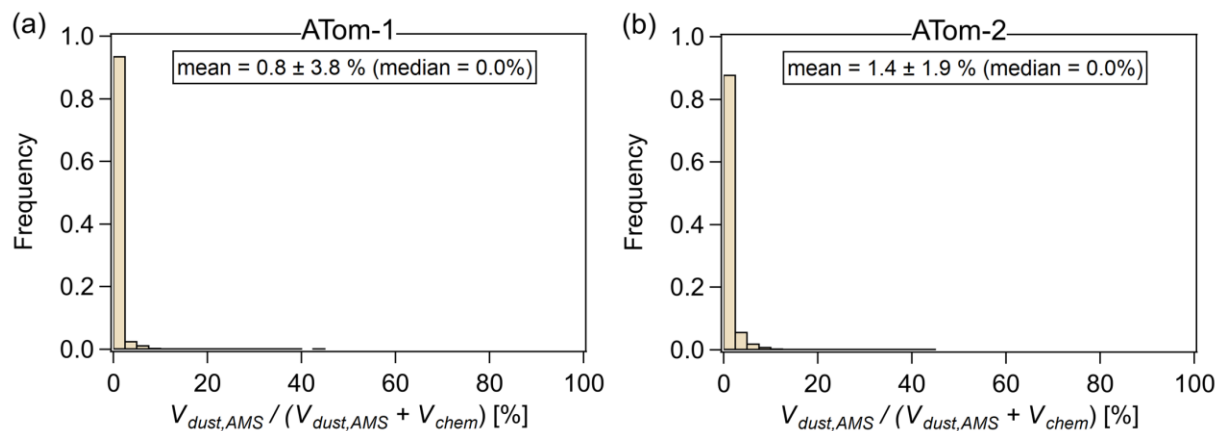


Fig. S22. Frequency distributions of submicron dust volume fraction for ATom-1 (left) and ATom-2 (right). $V_{dust,AMS}$ is calculated by applying the AMS transmission curve to the PALMS dust volume.

14. Particle size ranges observed by a suite of ATom aerosol instruments

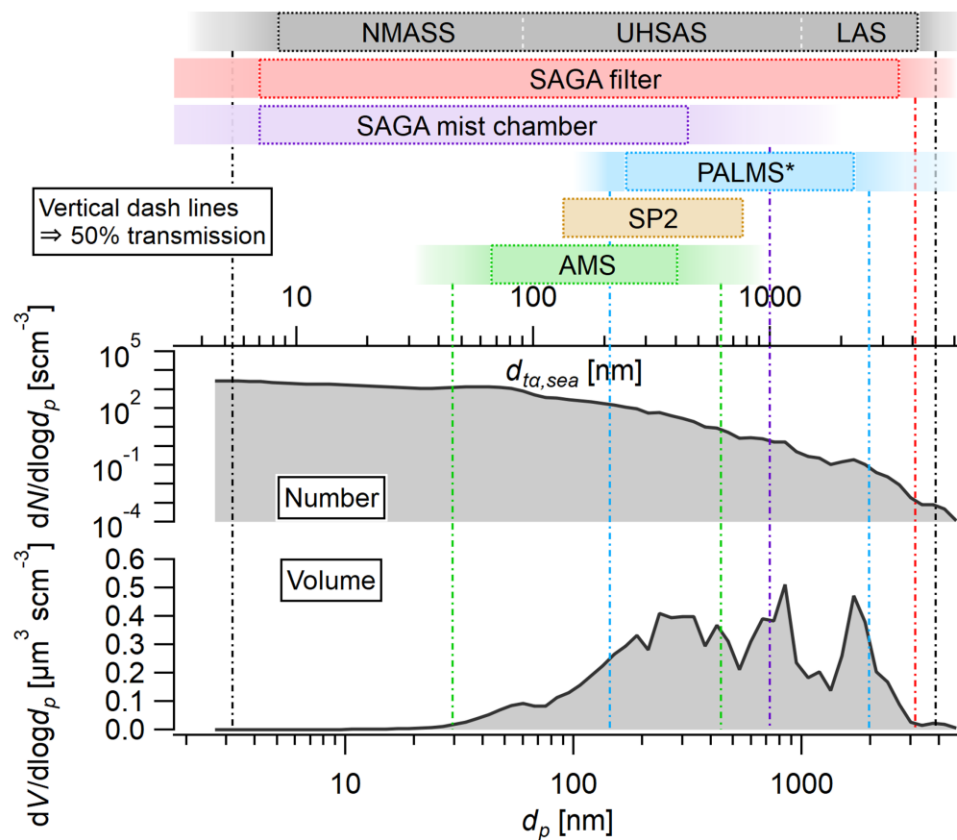


Fig. S23: Same as Fig. 1 in the main text except for showing the number size distribution in a log scale.

15. URG PM₁ cyclones, MOUDI 1 μm stage impactor transmissions

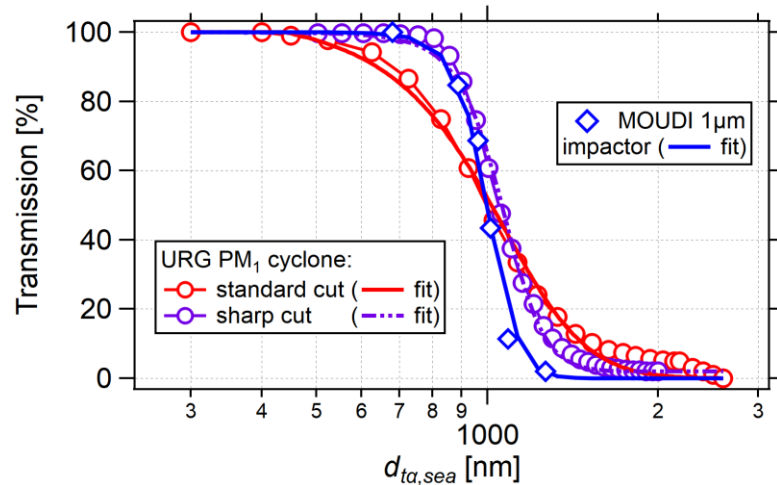


Fig. S24: The transmissions of URG PM₁ standard cut (Model: URG-2000-30EHB) and sharp cut (Model: SCC 2.229) cyclones, and MOUDI 1 μm stage impactor vs. transition-regime aerodynamic diameter ($d_{ta,sea}$; as the size range of interest to this study is in the transition regime, requiring a “slip correction”). The MOUDI experimental data is retrieved from Fig. 5 in Marple et al., (1991) using the Data Thief software (version 1.7). The d_{50} (corresponding d_{ta} at 50% transmissions) for this stage at $P = 1013$ mbar, $T = 293$ K, and a flow rate of 30 L m^{-3} was reported to be 1.00 μm (Marple et al., 1991). Similarly, the URG experimental data are retrieved from an official URG specification sheet for the standard cut version (<http://www.urgcorp.com/images/PDF%20Files/Resources/Cutsheets/URG-2000-30EHB.pdf>; last accessed on July 1st, 2019) and a technical report from BGI Inc for the sharp cut version (https://bgi.mesalabs.com/wp-content/uploads/sites/35/2015/02/scc_btr-2.229.pdf; last accessed on July 1st, 2019). We assume the aerodynamic diameters from the two reports applied the Cunningham slip corrections (C_c) for the transition regime size range since the slip correction factor, 1.166, is not negligible at 1 μm (and C_c increases non-linearly as the particle size decreases). The d_{50} is estimated to be 1010 nm and 1050 nm for the standard cut and the sharp cut cyclones, respectively.

16. Predicted decrease in aerosol size when dried from ambient condition

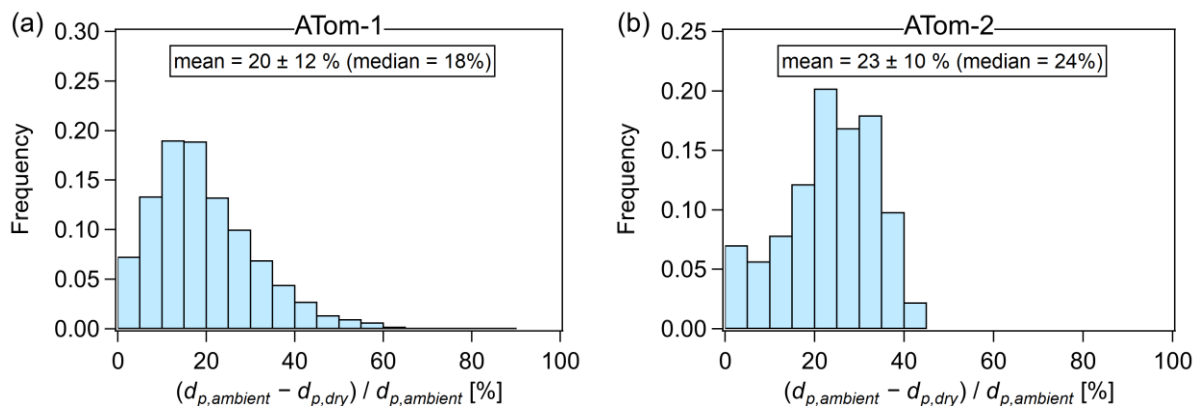


Fig. S25: Frequency distributions of the decrease in particle size if the particles lose liquid water content completely due to sample line heating: (a) ATom-1 and (b) ATom-2. The water associated with particulate inorganic species is predicted with AMS plus SAGA-MC aerosol composition (AMS SO_4 and NH_4 , SAGA-MC total nitrate ($\text{pNO}_3 + \text{HNO}_3$)) and E-AIM thermodynamic model (Clegg et al., 1998a, 1998b, 2003; Wexler, 2002; Friese and Ebel, 2010), and the water associated with organics is predicted using Eq. 5 in Guo et al. (2015) (Petters and Kreidenweis, 2007) with the AMS inferred ρ_{OA} from this study and organic hygroscopicity parameter (κ_{OA}) of 0.2 from literature for aged OA (Jimenez et al., 2009; Cerully et al., 2015).

17. The effect of aerosol density on AMS, URG PM₁ cyclones, and MOUDI 1 μm stage impactor transmissions

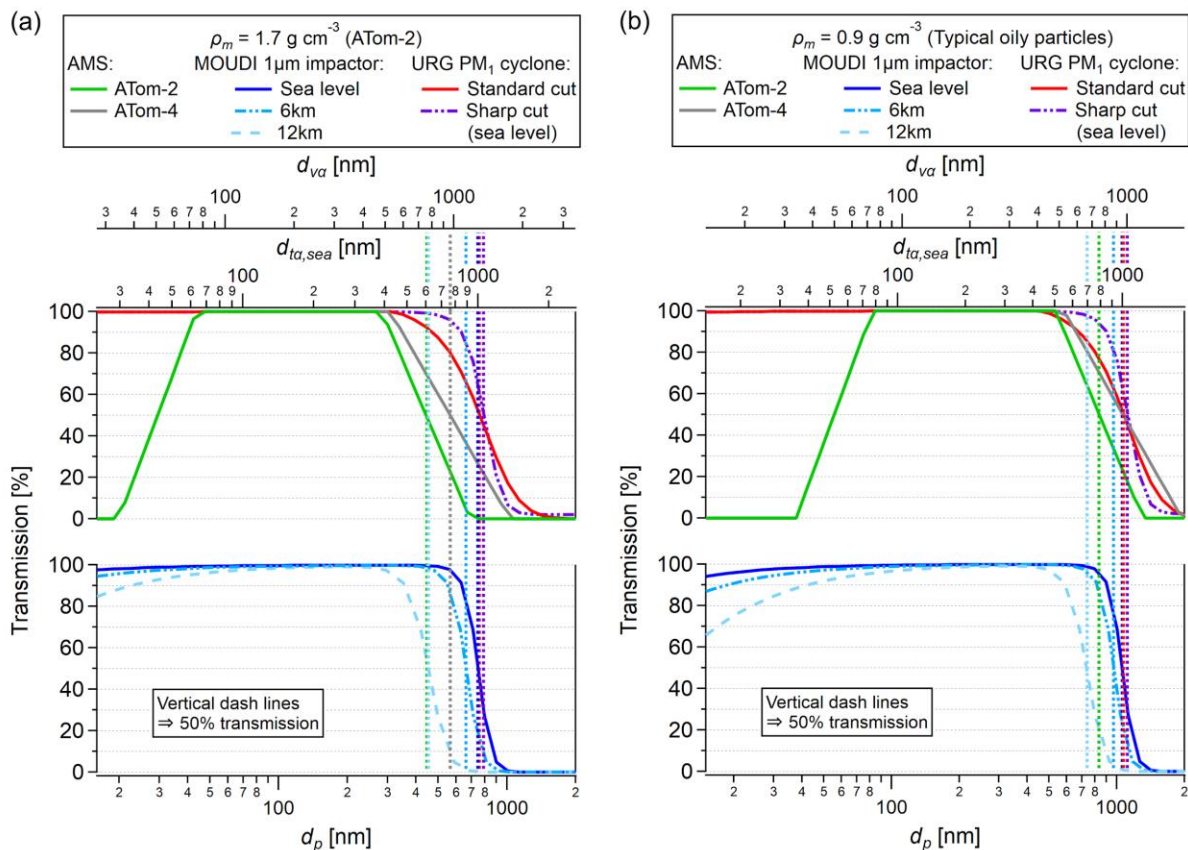


Fig. S26: The transmission curves of AMS (valid up to ~9 km and expected a similar performance at the max altitude), URG PM₁ cyclones operated at sea level, MOUDI 1 μm stage impactor operated at sea level (i.e., $P = 1013$ mbar), 6 km, and 12 km (at $T = 293$ K, typical cabin temperature and P based on the U.S. standard atmosphere) (NOAA, NASA, U. S. Air Force, 1976). (a) Results with an aerosol density of 1.7 g cm^{-3} , estimated from ATom-2 (ATom-1 is similar); (b) Results calculated with an aerosol density of 0.9 g cm^{-3} (typical of oily particles encountered on some laboratory and field studies) (Kuwata et al., 2012; Herring et al., 2015). The contrast in (a) and (b) illustrates the effects of aerosol density on the conversions between geometric diameter (d_p), vacuum aerodynamic diameter (d_{va}), and aerodynamic diameter (d_{ta} ; for the MOUDI impactor and URG cyclone; note that the MOUDI 6 km and 12 km profiles are slightly off at the plotted $d_{ta,sea}$ axis but precise at d_p and d_{va} axes; the cut sizes for AMS, URG, and MOUDI are summarized in Table S1). It also shows that the AMS cutoff size in d_{ta} depends on aerosol density (also altitude, see Table S1 for examples) and the MOUDI impactor cut size depends on altitude.

18. Volume closure: V_{chem} vs. $V_{phys,AMS}$

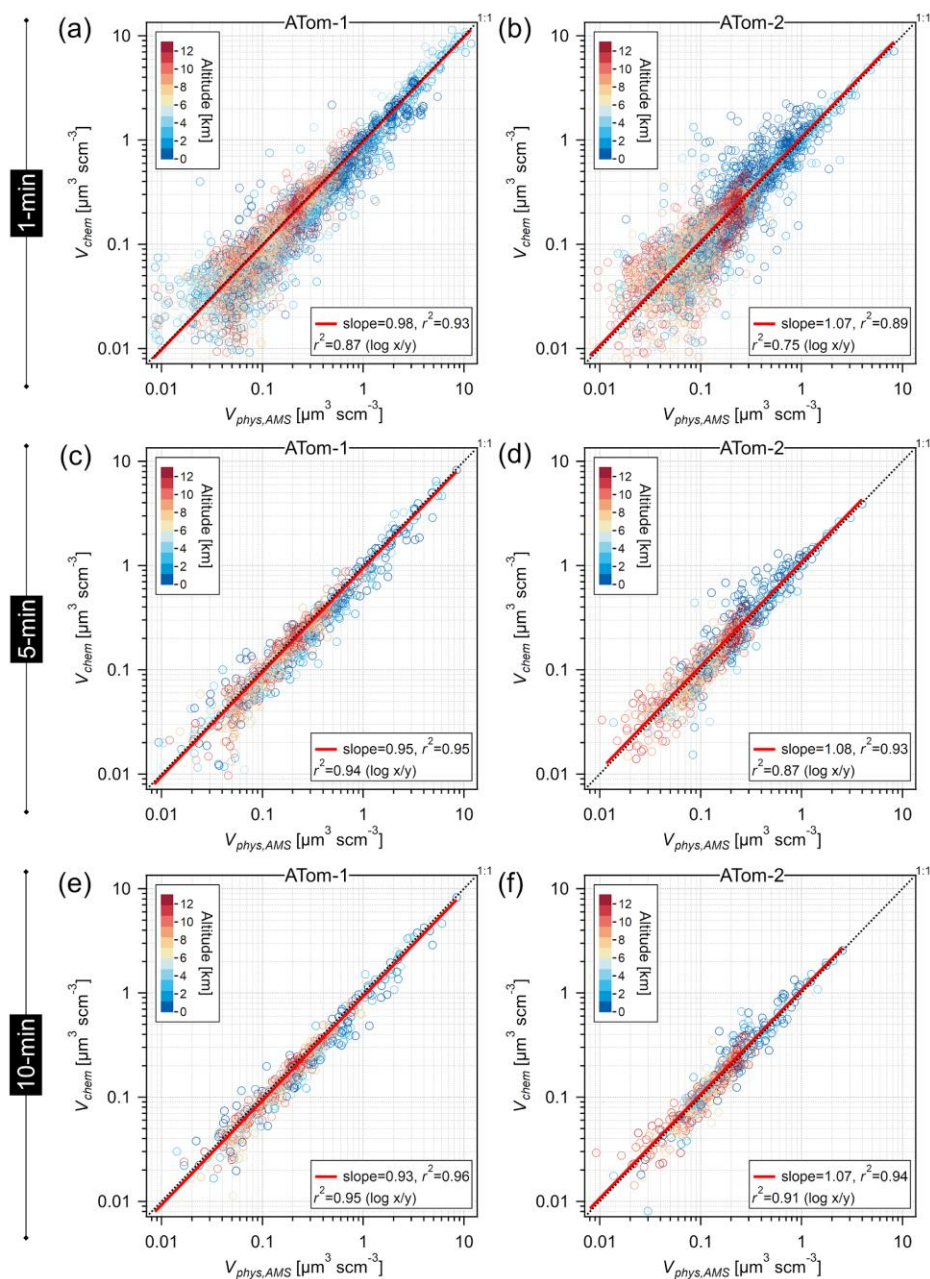


Fig. S27: Comparison between V_{chem} and $V_{phys,AMS}$ for ATom-1 (left) and ATom-2 (right), data points colored by altitude. The top, middle, and bottom panels are averaged by a time scale of 1, 5, and 10 min, respectively. Random noise is smoothed out at a longer averaging time scale.

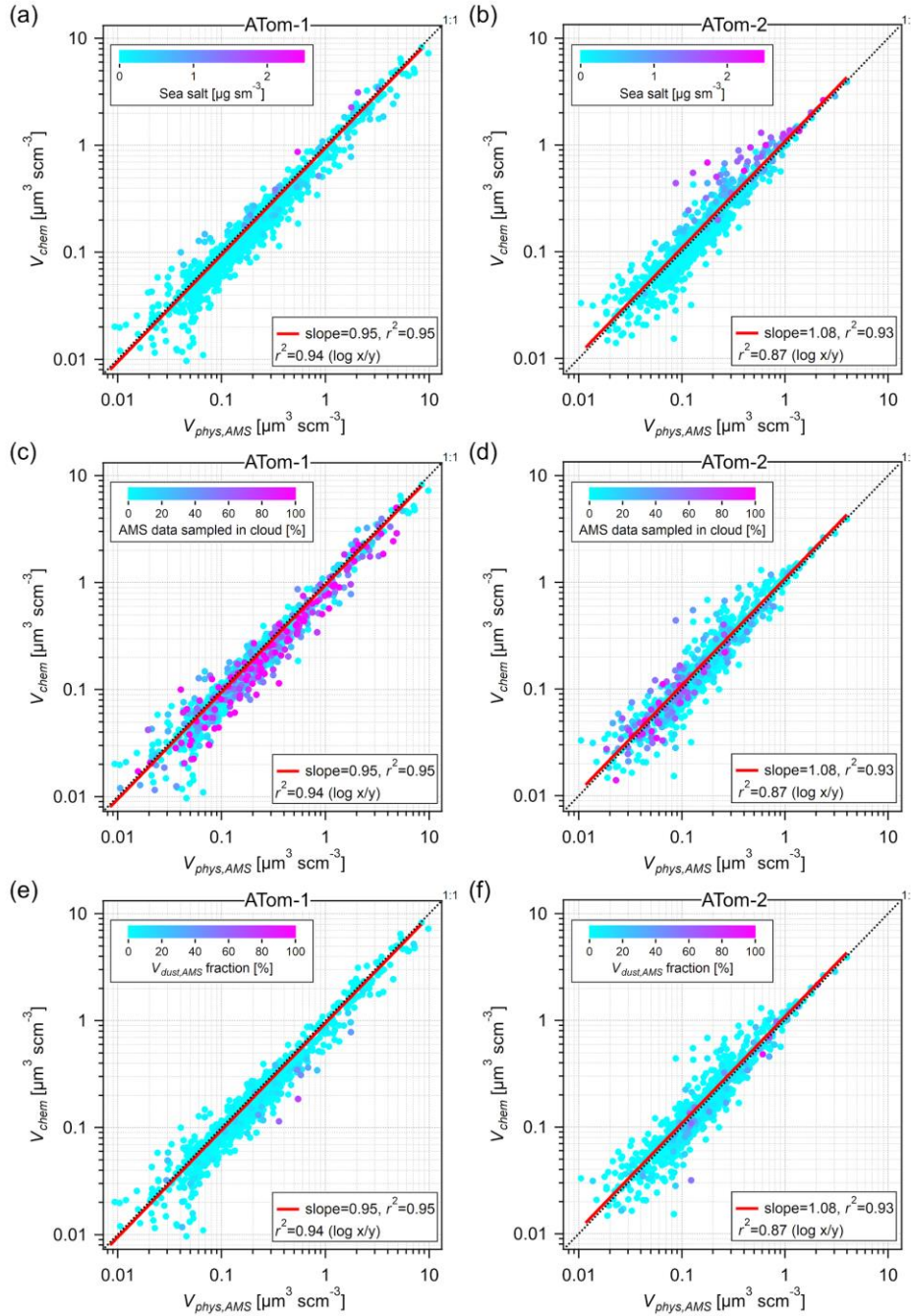


Fig. S28: Comparison between V_{chem} and $V_{phys,AMS}$ for ATom-1 (left) and ATom-2 (right) at 5-min average level. The top, middle, and bottom panels are colored by sea salt, the fraction of data sampled in clouds (the cloud indicator is from the 2nd generation Cloud, Aerosol, and Precipitation Spectrometer, CAPS) (Brock et al., 2019; Spanu et al., 2020), and submicron dust volume fraction (Fig. S22), respectively. For the intercomparison, we used 1 min AMS data, for which the raw mass spectra were averaged prior to data reduction and analysis. During the step, the spectra

collected in the clouds were not removed. In contrast, the AMP size distribution was averaged from 1 s data with exclusion of cloud impacts (i.e., 13% of the AMS data coverage). Therefore, there could be deviation derived from the way the raw data is processed and the impacts are investigated via panel (c) and (d).

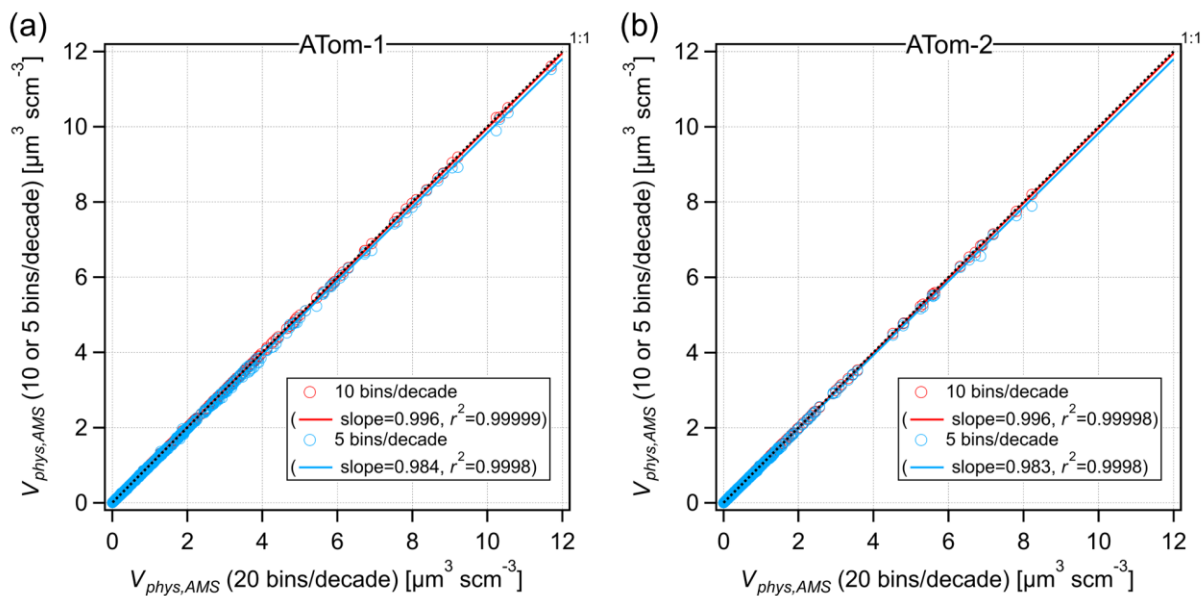


Fig. S29: Comparison of $V_{phys,AMS}$ calculated with different size resolutions for (a) ATom-1 and (b) ATom-2. The AMP size distribution is first converted to the broader bin width, i.e. 10 or 5 bins/decade vs. the reported AMP 20 bins/decade size resolution, and then the AMS inlet transmission is applied. The difference is minor in the ATom-1&2 cases since the AMP size distribution is relatively flat in the upper end AMS transmission size range (see Fig. 3 in the main text for instance).

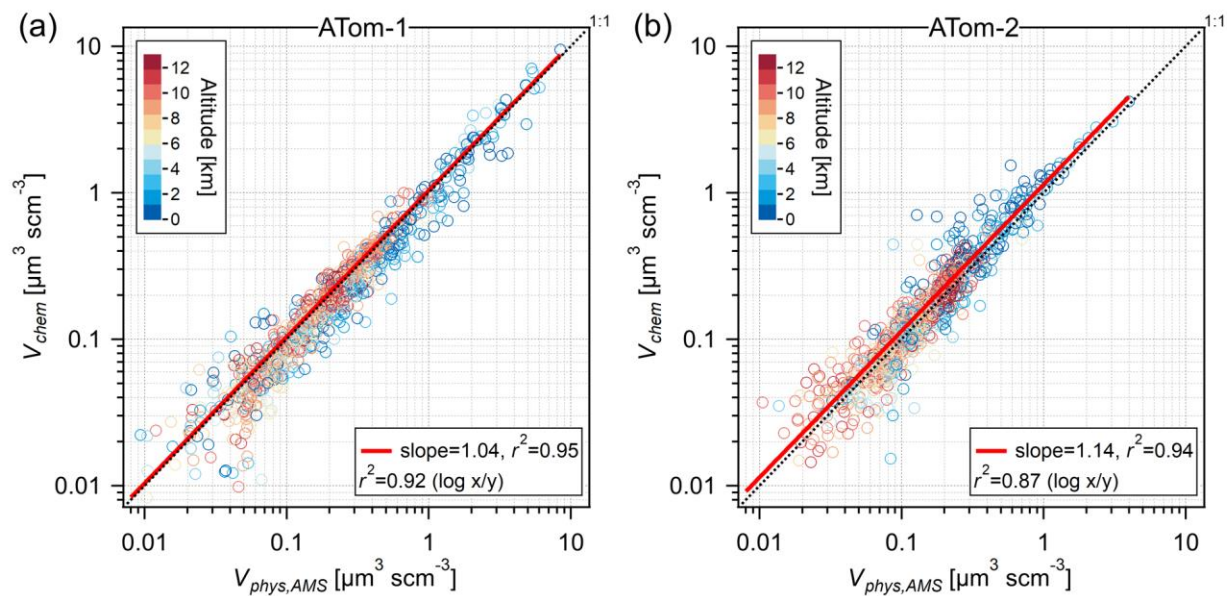


Fig. S30: Comparison between V_{chem} and $V_{phys,AMS}$ for (a) ATom-1 and (b) ATom-2. Data points are colored by altitude and averaged to 5 min resolution. Compared to Fig. 4 (main text), the plotted V_{chem} is recalculated by subtracting the AMS estimated ρ_{OA} with 0.2 g cm^{-3} , for a sensitivity test while keeping the other volumes the same.

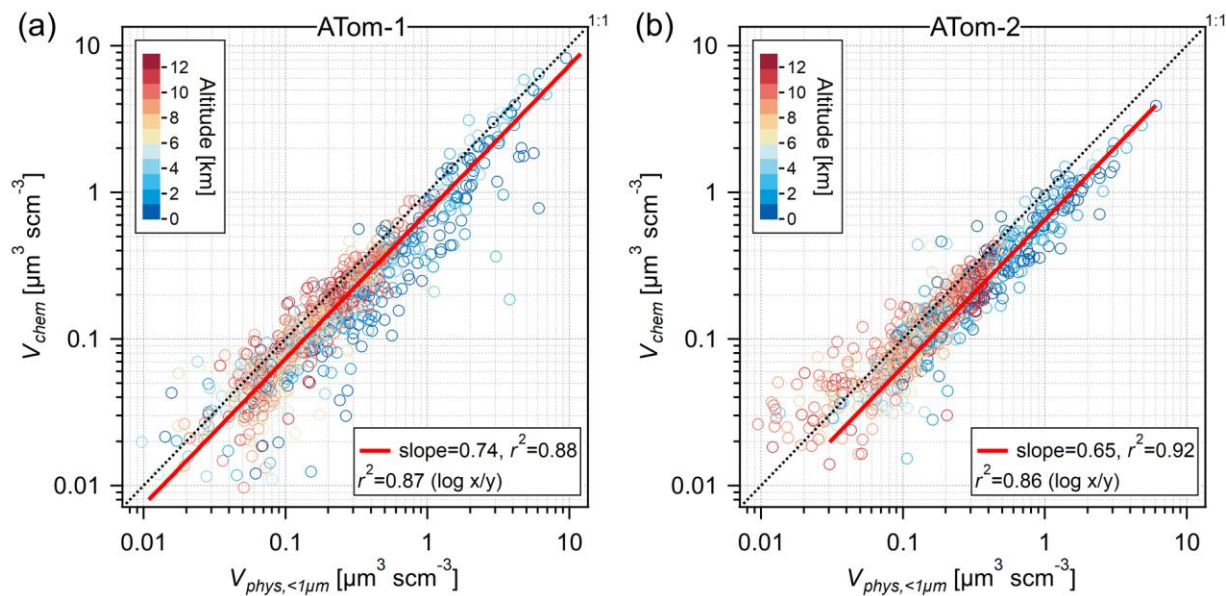


Fig. S31: Comparison between V_{chem} and $V_{phys, <1\mu m}$ for (a) ATom-1 and (b) ATom-2. Compared to Fig. 4 (main text), the plotted $V_{phys, <1\mu m}$ is truncated at $1 \mu m$ (d_p) of V_{phys} to simulate a simpler comparison of volume concentrations without applying AMS transmission profile. Data points are colored by altitude and averaged to 5 min resolution.

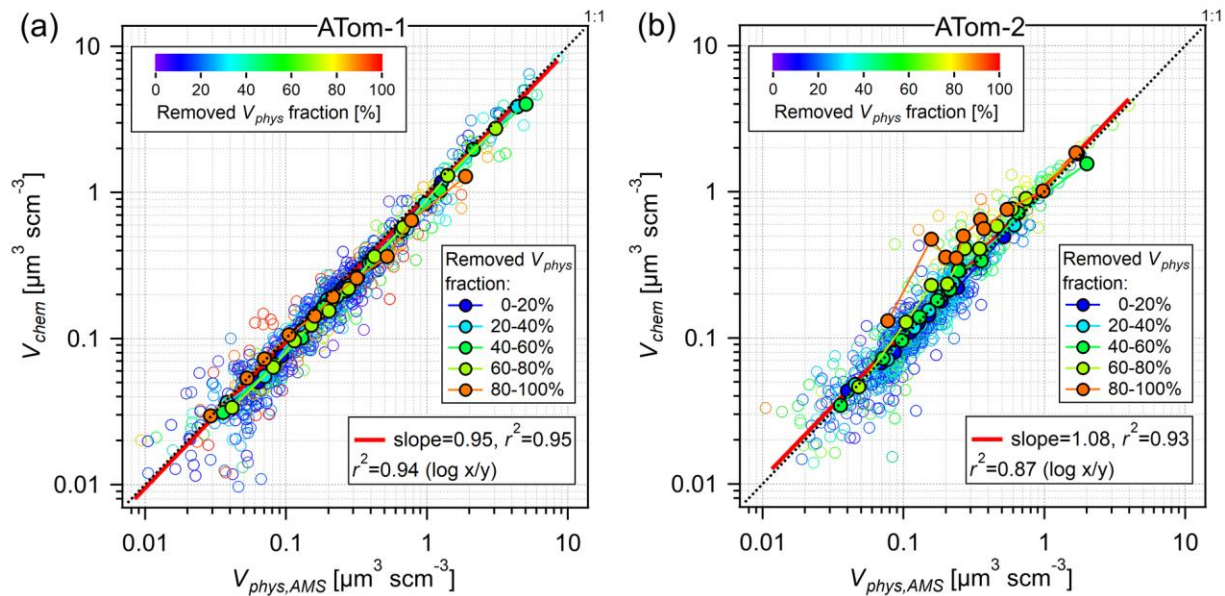


Fig. S32: Comparison between V_{chem} and $V_{phys,AMS}$ for ATom-1 (a) and ATom-2 (b), data points colored by the fraction of V_{phys} removed when applying the AMS transmission. The data points (marker only) are binned by a 20% interval based on the fraction and plotted with the 10th to 90th percentiles in each bin (line and marker) to investigate if any systematic bias exists.

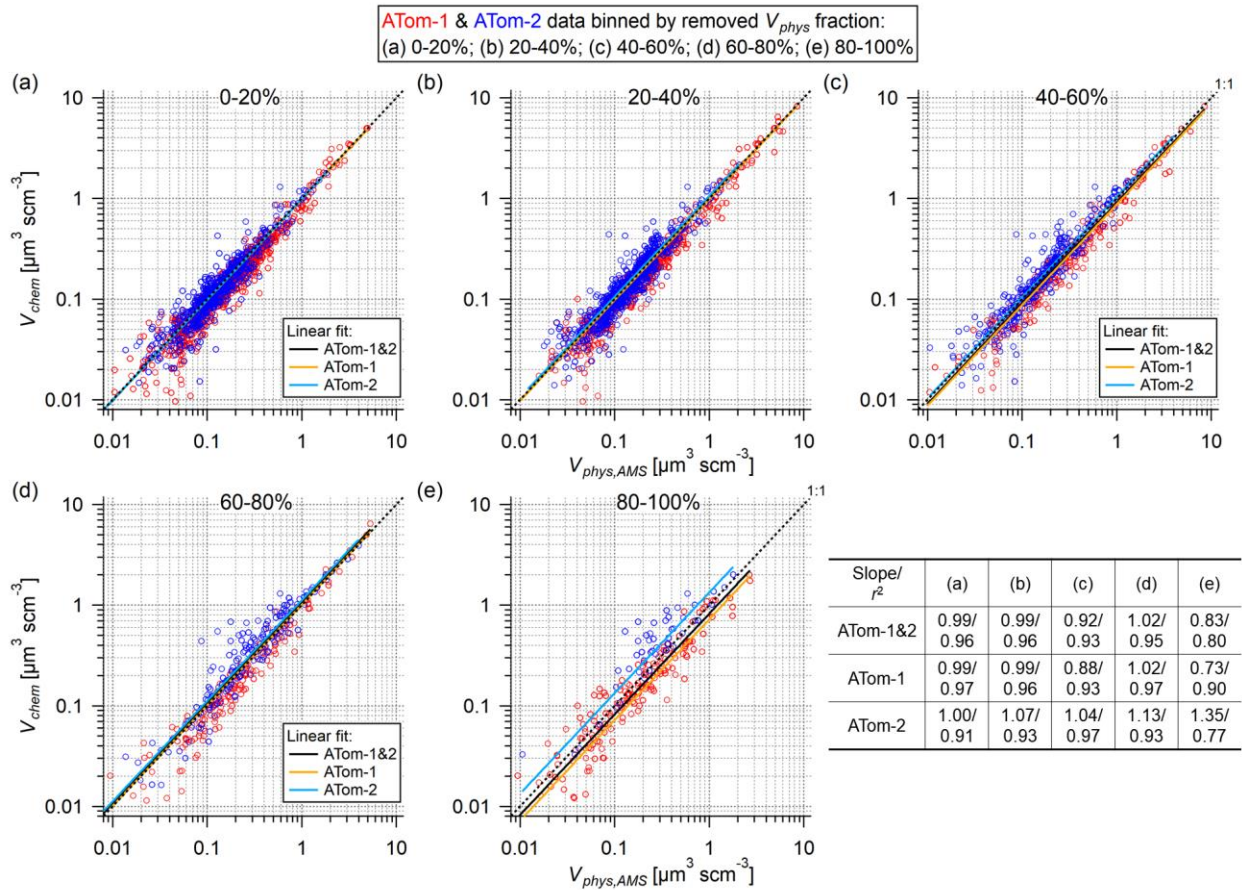


Fig. S33: Comparisons between V_{chem} and $V_{phys,AMS}$ for ATom-1 (blue color) and -2 (red color) data binned by the fraction of V_{phys} removed when applying AMS transmission: (a) 0-20%, (b) 20-40%, (c) 40-60%, (d) 60-80%, (e) 80-100%, respectively. The regressions and correlations are shown for the two ATom studies separately as well as for the combined data set.

19. Observable particle size range ranges of the AMP, SAGA filter, MOUDI 1 μ m stage impactor, AMS, and PALMS (ATom-1)

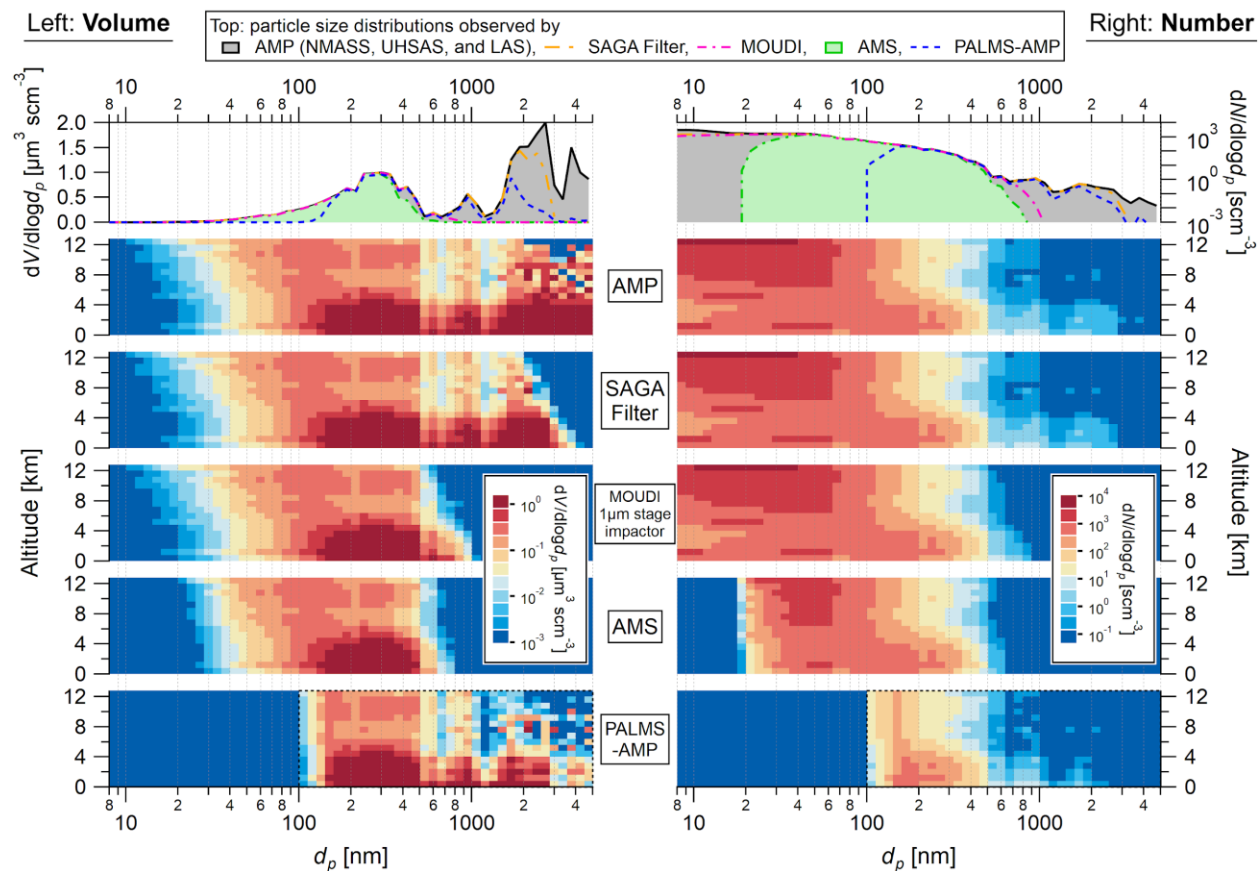


Fig. S34: Campaign-averaged volume (left) and number (right) size distributions observed by AMP in ATom-1 (NMASS measured down to 3 nm and here we only show the subrange starting from 8 nm), together with the approximate particle size ranges contributing chemical composition information (without consideration of the details of the chemical detection) to the AMS, PALMS, and SAGA filter, and size-selected by a MOUDI 1 μ m stage impactor. The top panel is one dimensional with the campaign average result of each instrument (the transmissions of MOUDI and SAGA filter are altitude dependent and plotted in Fig. 3 and Fig. S19, respectively; PALMS effective detection range depends on counting statistics, and the detected particles given a sampling period are discussed in Fig. S15-16). Note that the top panel shows the fraction of the average, while Fig. 8 (main text) shows the average fractions (a summary at Table S2). The right plots represent the size ranges of the number size distribution contributing chemical composition information to each instrument. The following panels show the vertical profiles of the same quantities for AMP, SAGA filter, MOUDI impactor, AMS, and PALMS-AMP, respectively. The

PALMS-AMP product (Froyd et al., 2019) reports composition above 100 nm, the size range indicated by the dashed square in the bottom panels. The plotted altitude bins are 800 m each.

20. Observable particle size range ranges for PALMS-AMP: comparing different size and time resolutions

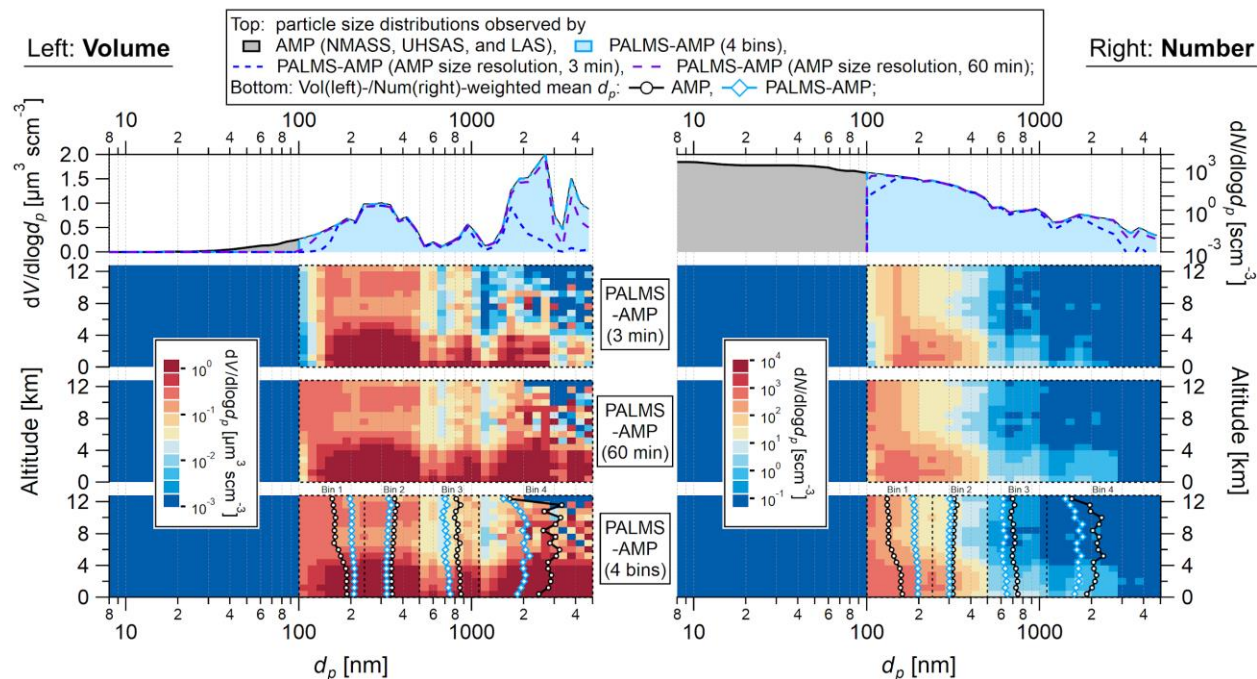


Fig. S35: Campaign-averaged volume (left) and number (right) size distributions observed by AMP in ATom-1, together with the approximate particle size ranges contributing chemical composition information to PALMS-AMP derived with three methods. Both the 3-min and 60-min panels are based on the reported AMP size resolution (as shown in Fig. S16. PALMS detected particle numbers within each AMP size bin are used to infer the fraction represented by PALMS-AMP. 100% is assigned to the bin if more than one particle is detected.), and the 4-bins PALMS-AMP product, supposed to have a full coverage of AMP above 100 nm (Froyd et al., 2019). A summary of the volume/number fraction vs. AMP (including other instruments) can be found at Table S2 and the vertical profiles are shown in the main text as Fig. 9g&o. The top panel is one dimensional with the campaign average result, and the rest are 2D vertical profiles. PALMS-AMP product (Froyd et al., 2019) reports above 100 nm, the size range indicated by the dashed square other than the top panel. All the plots represent the size ranges contributing chemical composition information to the PALMS-AMP based on the fractional aerosol population detected by PALMS. In the bottom panels, the volume-weighted (left) or number-weighted (right) diameters for the 4 larger bins (Froyd et al., 2019) are calculated for AMP only and PALMS-AMP, which illustrates

the shifted weighting on the aerosol population reported by the PALMS-AMP product due to the uneven PALMS relative data coverage as shown in Fig. S13.

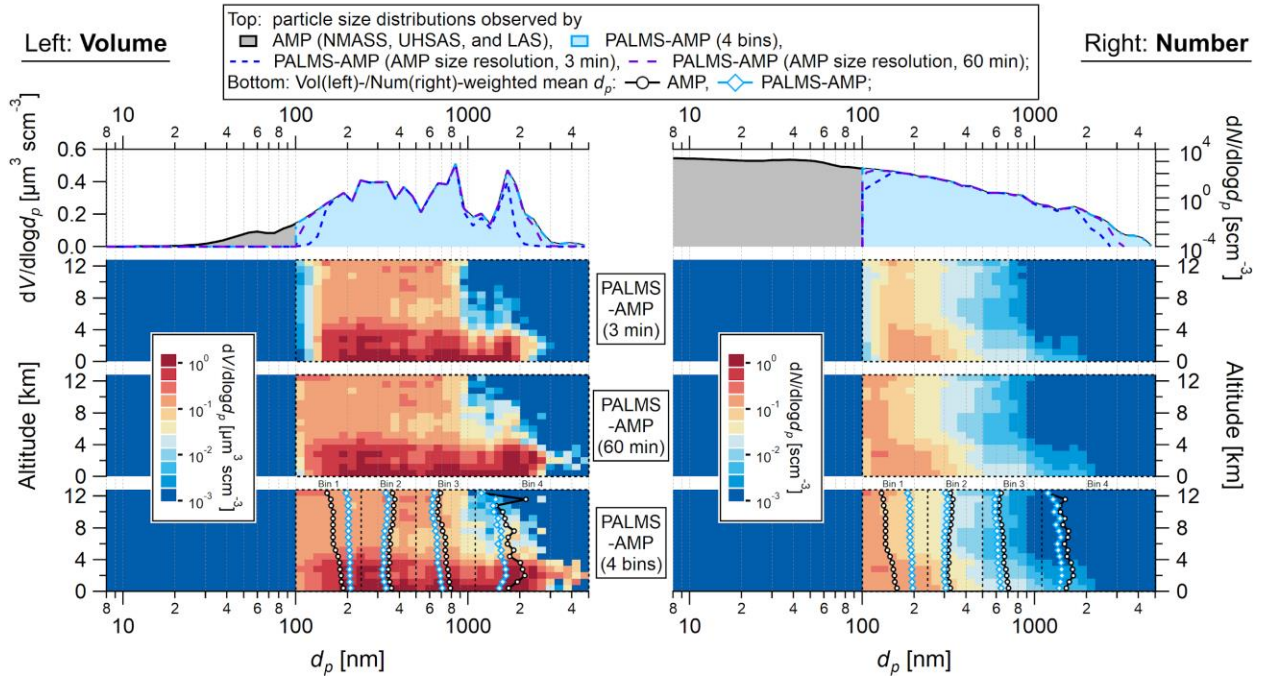


Fig. S36: Same as Fig. S35 but for ATom-2.

References

- Bahreini, R., Dunlea, E. J., Matthew, B. M., Simons, C., Docherty, K. S., DeCarlo, P. F., Jimenez, J. L., Brock, C. A. and Middlebrook, A. M.: Design and Operation of a Pressure-Controlled Inlet for Airborne Sampling with an Aerodynamic Aerosol Lens, *Aerosol Sci. Technol.*, 42(6), 465–471, doi:10.1080/02786820802178514, 2008.
- Bahreini, R., Ervens, B., Middlebrook, A. M., Warneke, C., de Gouw, J. A., DeCarlo, P. F., Jimenez, J. L., Brock, C. A., Neuman, J. A., Ryerson, T. B., Stark, H., Atlas, E., Brioude, J., Fried, A., Holloway, J. S., Peischl, J., Richter, D., Walega, J., Weibring, P., Wollny, A. G. and Fehsenfeld, F. C.: Organic aerosol formation in urban and industrial plumes near Houston and Dallas, Texas, *J. Geophys. Res.*, 114, D00F16, doi:10.1029/2008JD011493, 2009.
- Barth, M. C., Cantrell, C. A., Brune, W. H., Rutledge, S. A., Crawford, J. H., Huntrieser, H., Carey, L. D., MacGorman, D., Weisman, M., Pickering, K. E., Bruning, E., Anderson, B., Apel, E., Biggerstaff, M., Campos, T., Campuzano-Jost, P., Cohen, R., Crouse, J., Day, D. A., Diskin, G., Flocke, F., Fried, A., Garland, C., Heikes, B., Honomichl, S., Hornbrook, R., Huey, L. G., Jimenez, J. L., Lang, T., Lichtenstern, M., Mikoviny, T., Nault, B., O'Sullivan, D., Pan, L. L., Peischl, J., Pollack, I., Richter, D., Riemer, D., Ryerson, T., Schlager, H., St. Clair, J., Walega, J., Weibring, P., Weinheimer, A., Wennberg, P., Wisthaler, A., Wooldridge, P. J. and Ziegler, C.: The Deep Convective Clouds and Chemistry (DC3) Field Campaign, *Bull. Am. Meteorol. Soc.*, 96(8), 1281–1309, doi:10.1175/BAMS-D-13-00290.1, 2015.
- Baumgardner, D. and Huebert, B.: The airborne aerosol inlet workshop: Meeting report, *J. Aerosol Sci.*, 24(6), 835–846, doi:10.1016/0021-8502(93)90050-J, 1993.
- Belyaev, S. P. and Levin, L. M.: Investigation of aerosol aspiration by photographing particle tracks under flash illumination, *J. Aerosol Sci.*, 3(2), 127–140, doi:10.1016/0021-8502(72)90149-8, 1972.
- Belyaev, S. P. and Levin, L. M.: Techniques for collection of representative aerosol samples, *J. Aerosol Sci.*, 5(4), 325–338, doi:10.1016/0021-8502(74)90130-X, 1974.
- Brock, C. A., Williamson, C., Kupc, A., Froyd, K. D., Erdesz, F., Wagner, N., Richardson, M., Schwarz, J. P., Gao, R.-S., Katich, J. M., Campuzano-Jost, P., Nault, B. A., Schroder, J. C., Jimenez, J. L., Weinzierl, B., Dollner, M., Bui, T. and Murphy, D. M.: Aerosol size distributions during the Atmospheric Tomography Mission (ATom): methods, uncertainties, and data products, *Atmos. Meas. Tech.*, 12(6), 3081–3099, doi:10.5194/amt-12-3081-2019, 2019.
- Canagaratna, M. R., Jayne, J. T., Jimenez, J. L., Allan, J. D., Alfarra, M. R., Zhang, Q., Onasch, T. B., Drewnick, F., Coe, H., Middlebrook, A., Delia, A., Williams, L. R., Trimborn, A. M., Northway, M. J., DeCarlo, P. F., Kolb, C. E., Davidovits, P. and Worsnop, D. R.: Chemical and microphysical characterization of ambient aerosols with the aerodyne aerosol mass spectrometer, *Mass Spectrom. Rev.*, 26(2), 185–222, doi:10.1002/mas.20115, 2007.
- Cerully, K. M., Bougiatioti, A., Hite, J. R., Jr., Guo, H., Xu, L., Ng, N. L., Weber, R. and Nenes, A.: On the link between hygroscopicity, volatility, and oxidation state of ambient and water-

soluble aerosols in the southeastern United States, *Atmos. Chem. Phys.*, 15(15), 8679–8694, doi:10.5194/acp-15-8679-2015, 2015.

Chen, S.-C., Tsai, C.-J., Wu, C.-H., Pui, D. Y. H., Onischuk, A. A. and Karasev, V. V.: Particle loss in a critical orifice, *J. Aerosol Sci.*, 38(9), 935–949, doi:10.1016/j.jaerosci.2007.06.010, 2007.

Clegg, S. L., Brimblecombe, P. and Wexler, A. S.: Thermodynamic Model of the System $\text{H}^+ - \text{NH}_4^+ - \text{Na}^+ - \text{SO}_4^{2-} - \text{NO}_3^- - \text{Cl}^- - \text{H}_2\text{O}$ at 298.15 K, *J. Phys. Chem. A*, 102(12), 2155–2171, doi:10.1021/jp973043j, 1998a.

Clegg, S. L., Brimblecombe, P. and Wexler, A. S.: Thermodynamic Model of the System $\text{H}^+ - \text{NH}_4^+ - \text{SO}_4^{2-} - \text{NO}_3^- - \text{H}_2\text{O}$ at Tropospheric Temperatures, *J. Phys. Chem. A*, 102, 2137–2154, 1998b.

Clegg, S. L., Seinfeld, J. H. and Edney, E. O.: Thermodynamic modelling of aqueous aerosols containing electrolytes and dissolved organic compounds. II. An extended Zdanovskii–Stokes–Robinson approach, *J. Aerosol Sci.*, 34(6), 667–690, doi:10.1016/S0021-8502(03)00019-3, 2003.

Cubison, M. J., Ortega, a. M., Hayes, P. L., Farmer, D. K., Day, D., Lechner, M. J., Brune, W. H., Apel, E., Diskin, G. S., Fisher, J. a., Fuelberg, H. E., Hecobian, A., Knapp, D. J., Mikoviny, T., Riemer, D., Sachse, G. W., Sessions, W., Weber, R. J., Weinheimer, a. J., Wisthaler, A. and Jimenez, J. L.: Effects of aging on organic aerosol from open biomass burning smoke in aircraft and laboratory studies, *Atmos. Chem. Phys.*, 11(23), 12049–12064, doi:10.5194/acp-11-12049-2011, 2011.

van Donkelaar, A., Martin, R. V., Leaitch, W. R., Macdonald, A. M., Walker, T. W., Streets, D. G., Zhang, Q., Dunlea, E. J., Jimenez, J. L., Dibb, J. E., Huey, L. G., Weber, R. and Andreae, M. O.: Analysis of aircraft and satellite measurements from the Intercontinental Chemical Transport Experiment (INTEX-B) to quantify long-range transport of East Asian sulfur to Canada, *Atmos. Chem. Phys.*, 8(11), 2999–3014, doi:10.5194/acp-8-2999-2008, 2008.

Friese, E. and Ebel, A.: Temperature Dependent Thermodynamic Model of the System $\text{H}^+ - \text{NH}_4^+ - \text{Na}^+ - \text{SO}_4^{2-} - \text{NO}_3^- - \text{Cl}^- - \text{H}_2\text{O}$, *J. Phys. Chem. A*, 114(43), 11595–11631, doi:10.1021/jp101041j, 2010.

Froyd, K. D., Murphy, D. M., Brock, C. A., Campuzano-Jost, P., Dibb, J. E., Jimenez, J. L., Kupc, A., Middlebrook, A. M., Schill, G. P., Thornhill, K. L., Williamson, C. J., Wilson, J. C. and Ziemba, L. D.: A new method to quantify mineral dust and other aerosol species from aircraft platforms using single-particle mass spectrometry, *Atmos. Meas. Tech.*, 12(11), 6209–6239, doi:10.5194/amt-12-6209-2019, 2019.

Guo, H., Xu, L., Bougiatioti, A., Cerully, K. M., Capps, S. L., Hite, J. R., Carlton, A. G., Lee, S. H., Bergin, M. H., Ng, N. L., Nenes, A. and Weber, R. J.: Fine-particle water and pH in the southeastern United States, *Atmos. Chem. Phys.*, 15(9), 5211–5228, doi:10.5194/acp-15-5211-2015, 2015.

Guo, H., Sullivan, A. P., Campuzano-Jost, P., Schroder, J. C., Lopez-Hilfiker, F. D., Dibb, J. E.,

Jimenez, J. L., Thornton, J. A., Brown, S. S., Nenes, A. and Weber, R. J.: Fine particle pH and the partitioning of nitric acid during winter in the northeastern United States, *J. Geophys. Res.*, 121(17), 10355–10376, doi:10.1002/2016jd025311, 2016.

Hermann, M., Stratmann, F., Wilck, M. and Wiedensohler, A.: Sampling Characteristics of an Aircraft-Borne Aerosol Inlet System, *J. Atmos. Ocean. Technol.*, 18(1), 7–19, doi:10.1175/1520-0426(2001)018<0007:SCOAAB>2.0.CO;2, 2001.

Herring, C. L., Faiola, C. L., Massoli, P., Sueper, D., Erickson, M. H., McDonald, J. D., Simpson, C. D., Yost, M. G., Jobson, B. T. and VanReken, T. M.: New Methodology for Quantifying Polycyclic Aromatic Hydrocarbons (PAHs) Using High-Resolution Aerosol Mass Spectrometry, *Aerosol Sci. Technol.*, 49(11), 1131–1148, doi:10.1080/02786826.2015.1101050, 2015.

Hinds, W. C.: *Aerosol Technology: Properties, Behavior, and Measurement of Airborne Particles (Second Edition)*, John Wiley & Sons., 2012.

Hodzic, A., Campuzano-Jost, P., Bian, H., Chin, M., Colarco, P. R., Day, D. A., Froyd, K. D., Heinold, B., Jo, D. S., Katich, J. M., Kodros, J. K., Nault, B. A., Pierce, J. R., Ray, E., Schacht, J., Schill, G. P., Schroder, J. C., Schwarz, J. P., Sueper, D. T., Tegen, I., Tilmes, S., Tsigaridis, K., Yu, P. and Jimenez, J. L.: Characterization of organic aerosol across the global remote troposphere: a comparison of ATom measurements and global chemistry models, *Atmos. Chem. Phys.*, 20(8), 4607–4635, doi:10.5194/acp-20-4607-2020, 2020.

Huffman, J. A., Jayne, J. T., Drewnick, F., Aiken, A. C., Onasch, T., Worsnop, D. R. and Jimenez, J. L.: Design, Modeling, Optimization, and Experimental Tests of a Particle Beam Width Probe for the Aerodyne Aerosol Mass Spectrometer, *Aerosol Sci. Technol.*, 39(12), 1143–1163, doi:10.1080/02786820500423782, 2005.

Hu, W., Campuzano-Jost, P., Day, D. A., Croteau, P., Canagaratna, M. R., Jayne, J. T., Worsnop, D. R. and Jimenez, J. L.: Evaluation of the new capture vaporizer for aerosol mass spectrometers (AMS) through field studies of inorganic species, *Aerosol Sci. Technol.*, 51(6), 735–754, doi:10.1080/02786826.2017.1296104, 2017.

Jacob, D. J., Crawford, J. H., Maring, H., Clarke, A. D., Dibb, J. E., Emmons, L. K., Ferrare, R. A., Hostetler, C. A., Russell, P. B., Singh, H. B., Thompson, A. M., Shaw, G. E., McCauley, E., Pederson, J. R. and Fisher, J. A.: The Arctic Research of the Composition of the Troposphere from Aircraft and Satellites (ARCTAS) mission: design, execution, and first results, *Atmos. Chem. Phys.*, 10(11), 5191–5212, doi:10.5194/acp-10-5191-2010, 2010.

Jimenez, J. L., Canagaratna, M. R., Donahue, N. M., Prevot, A. S. H., Zhang, Q., Kroll, J. H., DeCarlo, P. F., Allan, J. D., Coe, H., Ng, N. L., Aiken, A. C., Docherty, K. S., Ulbrich, I. M., Grieshop, A. P., Robinson, A. L., Duplissy, J., Smith, J. D., Wilson, K. R., Lanz, V. A., Hueglin, C., Sun, Y. L., Tian, J., Laaksonen, A., Raatikainen, T., Rautiainen, J., Vaattovaara, P., Ehn, M., Kulmala, M., Tomlinson, J. M., Collins, D. R., Cubison, M. J., Dunlea, E. J., Huffman, J. A., Onasch, T. B., Alfarra, M. R., Williams, P. I., Bower, K., Kondo, Y., Schneider, J., Drewnick, F., Borrmann, S., Weimer, S., Demerjian, K., Salcedo, D., Cottrell, L., Griffin, R., Takami, A., Miyoshi, T., Hatakeyama, S., Shimono, A., Sun, J. Y., Zhang, Y. M., Dzepina, K., Kimmel, J. R.,

Sueper, D., Jayne, J. T., Herndon, S. C., Trimborn, A. M., Williams, L. R., Wood, E. C., Middlebrook, A. M., Kolb, C. E., Baltensperger, U. and Worsnop, D. R.: Evolution of organic aerosols in the atmosphere, *Science*, 326(5959), 1525–1529, doi:10.1126/science.1180353, 2009.

Knote, C., Brunner, D., Vogel, H., Allan, J., Asmi, A., Äijälä, M., Carbone, S., Gon, H. D. van der, Jimenez, J. L., Kiendler-Scharr, A., Mohr, C., Poulain, L., Prévôt, A. S. H., Swietlicki, E. and Vogel, B.: Towards an online-coupled chemistry-climate model: evaluation of trace gases and aerosols in COSMO-ART, *Geosci. Model Dev.*, 4(4), 1077–1102, doi:10.5194/gmd-4-1077-2011, 2011.

Kumar, P., Nenes, A. and Sokolik, I. N.: Importance of adsorption for CCN activity and hygroscopic properties of mineral dust aerosol, *Geophys. Res. Lett.*, 36(24), L23804, doi:10.1029/2009GL040827, 2009a.

Kumar, P., Sokolik, I. N. and Nenes, A.: Parameterization of cloud droplet formation for global and regional models: including adsorption activation from insoluble CCN, *Atmos. Chem. Phys.*, 9(7), 2517–2532, doi:10.5194/acp-9-2517-2009, 2009b.

Kuwata, M., Zorn, S. R. and Martin, S. T.: Using elemental ratios to predict the density of organic material composed of carbon, hydrogen, and oxygen, *Environ. Sci. Technol.*, 46(2), 787–794, doi:10.1021/es202525q, 2012.

Marple, V., Olson, B., Romay, F., Hudak, G., Geerts, S. M. and Lundgren, D.: Second Generation Micro-Orifice Uniform Deposit Impactor, 120 MOUDI-II: Design, Evaluation, and Application to Long-Term Ambient Sampling, *Aerosol Sci. Technol.*, 48(4), 427–433, doi:10.1080/02786826.2014.884274, 2014.

Marple, V. A., Rubow, K. L. and Behm, S. M.: A Microorifice Uniform Deposit Impactor (MOUDI): Description, Calibration, and Use, *Aerosol Sci. Technol.*, 14(4), 434–446, doi:10.1080/02786829108959504, 1991.

McFarland, A. R., Gong, H., Muyschondt, A., Wentz, W. B. and Anand, N. K.: Aerosol Deposition in Bends with Turbulent Flow, *Environ. Sci. Technol.*, 31(12), 3371–3377, doi:10.1021/es960975c, 1997.

McNaughton, C. S., Clarke, A. D., Howell, S. G., Pinkerton, M., Anderson, B., Thornhill, L., Hudgins, C., Winstead, E., Dibb, J. E., Scheuer, E. and Maring, H.: Results from the DC-8 Inlet Characterization Experiment (DICE): Airborne Versus Surface Sampling of Mineral Dust and Sea Salt Aerosols, *Aerosol Sci. Technol.*, 41(2), 136–159, doi:10.1080/02786820601118406, 2007.

Middlebrook, A. M., Bahreini, R., Jimenez, J. L. and Canagaratna, M. R.: Evaluation of Composition-Dependent Collection Efficiencies for the Aerodyne Aerosol Mass Spectrometer using Field Data, *Aerosol Sci. Technol.*, 46(3), 258–271, doi:10.1080/02786826.2011.620041, 2012.

Molleker, S., Helleis, F., Klimach, T., Appel, O., Clemen, H.-C., Dragoneas, A., Gurk, C., Hünig, A., Köllner, F., Rubach, F., Schulz, C., Schneider, J. and Borrmann, S.: Application of an O-ring

pinch device as a constant-pressure inlet (CPI) for airborne sampling, *Atmos. Meas. Tech.*, 13(7), 3651–3660, doi:10.5194/amt-13-3651-2020, 2020.

Murphy, D. M., Froyd, K. D., Brock, C. A., Williamson, C. and Kupc, A.: Interactive comment on “The Importance of Size Ranges in Aerosol Instrument Intercomparisons: A Case Study for the ATom Mission” by Hongyu Guo et al, *Atmos. Meas. Tech. Discuss.* [online] Available from: https://editor.copernicus.org/index.php/amt-2020-224-SC1.pdf?_mdl=msover_md&_jrl=400&_lcm=oc108lcm109w&_acm=get_comm_file&_ms=86223&c=183914&salt=1135168063444623208, 2020.

Nenes, A., Murray, B. and Bougiatioti, A.: Mineral Dust and its Microphysical Interactions with Clouds, in *Mineral Dust: A Key Player in the Earth System*, edited by P. Knippertz and J. B. Stuut, pp. 287–325, Springer, Dordrecht., 2014.

NOAA, NASA, U. S. Air Force: U. S. Standard Atmosphere 1976, U. S. Government Printing Office, Washington, DC., 1976.

Peck, J., Gonzalez, L. A., Williams, L. R., Xu, W., Croteau, P. L., Timko, M. T., Jayne, J. T., Worsnop, D. R., Miake-Lye, R. C. and Smith, K. A.: Development of an aerosol mass spectrometer lens system for PM_{2.5}, *Aerosol Sci. Technol.*, 50(8), 781–789, doi:10.1080/02786826.2016.1190444, 2016.

Petters, M. D. and Kreidenweis, S. M.: A single parameter representation of hygroscopic growth and cloud condensation nucleus activity, *Atmos. Chem. Phys.*, 7(8), 1961–1971, doi:10.5194/acp-7-1961-2007, 2007.

Pieber, S. M., El Haddad, I., Slowik, J. G., Canagaratna, M. R., Jayne, J. T., Platt, S. M., Bozzetti, C., Daellenbach, K. R., Fröhlich, R., Vlachou, A., Klein, F., Dommen, J., Miljevic, B., Jiménez, J. L., Worsnop, D. R., Baltensperger, U. and Prévôt, A. S. H.: Inorganic Salt Interference on CO₂⁺ in Aerodyne AMS and ACSM Organic Aerosol Composition Studies, *Environ. Sci. Technol.*, 50(19), 10494–10503, doi:10.1021/acs.est.6b01035, 2016.

Porter, J. N., Clarke, A. D., Ferry, G. and Pueschel, R. F.: Aircraft studies of size-dependent aerosol sampling through inlets, *J. Geophys. Res.*, 97(D4), 3815–3824, doi:10.1029/91jd02886, 1992.

Pui, D. Y. H., Romay-Novas, F. and Liu, B. Y. H.: Experimental Study of Particle Deposition in Bends of Circular Cross Section, *Aerosol Sci. Technol.*, 7(3), 301–315, doi:10.1080/02786828708959166, 1987.

Rogers, D.: HIAPER Modular Inlet, [online] Available from: <https://www.eol.ucar.edu/instruments/hiaper-modular-inlet> (Accessed 4 June 2020), 2011.

Schreiner, J., Schild, U., Voigt, C. and Mauersberger, K.: Focusing of aerosols into a particle beam at pressures from 10 to 150 Torr, *Aerosol Sci. Technol.*, 31(5), 373–382, 1999.

Sheridan, P. J. and Norton, R. B.: Determination of the passing efficiency for aerosol chemical species through a typical aircraft-mounted, diffuser-type aerosol inlet system, *J. Geophys. Res.*,

103(D7), 8215–8225, doi:10.1029/98JD00286, 1998.

Shilling, J. E., Chen, Q., King, S. M., Rosenoern, T., Kroll, J. H., Worsnop, D. R., DeCarlo, P. F., Aiken, A. C., Sueper, D., Jimenez, J. L. and Martin, S. T.: Loading-dependent elemental composition of α -pinene SOA particles, *Atmos. Chem. Phys.*, 9(3), 771–782, doi:10.5194/acp-9-771-2009, 2009.

Spanu, A., Dollner, M., Gasteiger, J., Bui, T. P. and Weinzierl, B.: Flow-induced errors in airborne in situ measurements of aerosols and clouds, *Atmos. Meas. Tech.*, 13(4), 1963–1987, doi:10.5194/amt-13-1963-2020, 2020.

Stith, J. L., Ramanathan, V., Cooper, W. a., Roberts, G. C., DeMott, P. J., Carmichael, G., Hatch, C. D., Adhikary, B., Twohy, C. H., Rogers, D. C., Baumgardner, D., Prenni, a. J., Campos, T., Gao, R., Anderson, J. and Feng, Y.: An overview of aircraft observations from the Pacific Dust Experiment campaign, *J. Geophys. Res.*, 114(D5), D05207, doi:10.1029/2008JD010924, 2009.

Toon, O. B., Maring, H., Dibb, J., Ferrare, R., Jacob, D. J., Jensen, E. J., Luo, Z. J., Mace, G. G., Pan, L. L., Pfister, L., Rosenlof, K. H., Redemann, J., Reid, J. S., Singh, H. B., Thompson, A. M., Yokelson, R., Minnis, P., Chen, G., Jucks, K. W. and Pszenny, A.: Planning, implementation, and scientific goals of the Studies of Emissions and Atmospheric Composition, Clouds and Climate Coupling by Regional Surveys (SEAC⁴RS) field mission, *J. Geophys. Res. Atmos.*, 121(9), 4967–5009, doi:10.1002/2015JD024297, 2016.

Vay, S. A., Anderson, B. E., Thornhill, K. L. and Hudgins, C. H.: An Assessment of Aircraft-Generated Contamination on In Situ Trace Gas Measurements: Determinations from Empirical Data Acquired Aloft, *J. Atmos. Ocean. Technol.*, 20, 1478–1487, doi: 10.1175/1520-0426(2003)020<1478:AAOACO>2.0.CO;2, 2003.

von der Weiden, S.-L., Drewnick, F. and Borrmann, S.: Particle Loss Calculator – a new software tool for the assessment of the performance of aerosol inlet systems, *Atmos. Meas. Tech.*, 2(2), 479–494, doi:10.5194/amt-2-479-2009, 2009.

Wexler, A. S.: Atmospheric aerosol models for systems including the ions H^+ , NH_4^+ , Na^+ , SO_4^{2-} , NO_3^- , Cl^- , Br^- , and H_2O , *J. Geophys. Res.*, 107(D14), 4207, doi:10.1029/2001JD000451, 2002.

Williams, L. R., Gonzalez, L. A., Peck, J., Trimborn, D., McInnis, J., Farrar, M. R., Moore, K. D., Jayne, J. T., Robinson, W. A., Lewis, D. K., Onasch, T. B., Canagaratna, M. R., Trimborn, A., Timko, M. T., Magoon, G., Deng, R., Tang, D., de la Rosa Blanco, E., Prévôt, A. S. H., Smith, K. A. and Worsnop, D. R.: Characterization of an aerodynamic lens for transmitting particles greater than 1 micrometer in diameter into the Aerodyne aerosol mass spectrometer, *Atmos. Meas. Tech.*, 6(11), 3271–3280, doi:10.5194/amt-6-3271-2013, 2013.

Williamson, C. J., Kupc, A., Axisa, D., Bilsback, K. R., Bui, T., Campuzano-Jost, P., Dollner, M., Froyd, K. D., Hodshire, A. L., Jimenez, J. L., Kodros, J. K., Luo, G., Murphy, D. M., Nault, B. A., Ray, E. A., Weinzierl, B., Wilson, J. C., Yu, F., Yu, P., Pierce, J. R. and Brock, C. A.: A large source of cloud condensation nuclei from new particle formation in the tropics, *Nature*, 574(7778), 399–403, doi:10.1038/s41586-019-1638-9, 2019.

Yang, Q., Easter, R. C., Campuzano-Jost, P., Jimenez, J. L., Fast, J. D., Ghan, S. J., Wang, H., Berg, L. K., Barth, M. C., Liu, Y., Shrivastava, M. B., Singh, B., Morrison, H., Fan, J., Ziegler, C. L., Bela, M., Apel, E., Diskin, G. S., Mikoviny, T. and Wisthaler, A.: Aerosol transport and wet scavenging in deep convective clouds: A case study and model evaluation using a multiple passive tracer analysis approach, *J. Geophys. Res. D: Atmos.*, 120(16), 8448–8468, doi:10.1002/2015JD023647, 2015.

Zhang, Q., Stanier, C. O., Canagaratna, M. R., Jayne, J. T., Worsnop, D. R., Pandis, S. N. and Jimenez, J. L.: Insights into the chemistry of new particle formation and growth events in Pittsburgh based on aerosol mass spectrometry, *Environ. Sci. Technol.*, 38(18), 4797–4809, doi:10.1021/es035417u, 2004a.

Zhang, X. F., Smith, K. A., Worsnop, D. R., Jimenez, J. L., Jayne, J. T., Kolb, C. E., Morris, J. and Davidovits, P.: Numerical characterization of particle beam collimation: Part II - Integrated aerodynamic-lens-nozzle system, *Aerosol Sci. Technol.*, 38(6), 619–638, 2004b.

Zíková, N., Ondráček, J. and Ždímal, V.: Size-Resolved Penetration Through High-Efficiency Filter Media Typically Used for Aerosol Sampling, *Aerosol Sci. Technol.*, 49(4), 239–249, doi:10.1080/02786826.2015.1020997, 2015.